Ion Probe Dating of Zircons from Wuluke Volcano, NW Tibet, China: Constraints on Magma Evolution

by

Katherine L. Cooper

A thesis submitted to the Graduate Faculty of
Auburn University
in partial fulfillment of the
requirements for the Degree of
Master of Science

Auburn, Alabama
May 8, 2016

Approved by

Haibo Zou, Chair, Associate Professor of Geosciences
Mark G. Steltenpohl, Professor of Geosciences
David T. King Jr., Professor of Geosciences

ABSTRACT

The Ashikule volcanic cluster (AVC) is located in the Ashikule basin, on top of the Kunlun Mountains in the NW Tibetan Plateau. There is very little research on the AVC, so further research is necessary in order to gain a better understanding of the volcanology and magmatic process associated with the northern Tibet plateau. The Wuluke volcano is located in the central east area of the AVC and it is currently covered in late Pleistocene to Holocene lava flows. These young volcanic rocks derive from a potassic melt and contain an abundance of zircon grains. Zircon has played a key role in geochronology and crustal evolution studies. Zircon xenocrysts have long been considered burdensome because they can hinder magmatic age estimation. However, a growing number of studies have shown that xenocrystic zircons can provide valuable information on magma evolution and crustal contamination. This research utilizes U-Pb dating methods and secondary ion mass spectrometry (SIMS) to date zircons from the Wuluke volcano, which can be used to provide constraints on magma evolution and contamination processes.

Measured zircons yielded multiple zircon age populations ranging from the most recent eruption to the Proterozoic. The Proterozoic ages correlate well with known country rock ages indicating that the sample contains both phenocryst and xenocryst zircons providing evidence that lavas from the Wuluke volcano have experienced crustal contamination through the assimilation of zircon-bearing country rocks. Electron microprobe analyses of orthopyroxene and plagioclase phenocrysts indicate that the early

formed phenocrysts remained in equilibrium with the melt and were not affected by crustal contamination.

AKNOWLEDGMENTS

Funding for this research was graciously provided by Haibo Zou through a National Science Foundation of China grant (41272070), by the Department of Geosciences through the Spencer Waters and Dan Folse Memorial award, and by the Auburn University Graduate School through a Graduate Research grant. Thanks are owed to Ming-Chang Liu of the University of California at Los Angeles (UCLA) for his guidance on the operation of SIMS. Thanks are owed to Chris Fleisher and the University of Georgia for providing the facilities and use of the electron microprobe, as well as instruction on the operation of the equipment. Thanks are owed to fellow graduate student Di Fan for transporting samples to the Langfang Geological Service Company in China. Special thanks are owed to Haibo Zou for providing funding, materials, valuable insights and knowledge into the field of research, assistance in sample preparation, and on the operation of SIMS. Thanks are also owed to thesis committee members Mark Steltenpohl and David T. King Jr. for their critiques and comments that improved the quality of this thesis. The ion microprobe facility at UCLA is partly supported by a grant from the Instrumentation and Facilities Program, Division of Earth Sciences, National Science Foundation. Finally, thanks are owed to my parents, Rick and Maria Spyker, and my husband, Tyler Cooper, for providing support throughout my undergraduate and graduate studies.

TABLE OF CONTENTS

LIST OF TABLES

LIST OF FIGURES

INTRODUCTION

The Ashikule volcanic cluster (AVC) is located in the Ashikule basin, set on top of the west Kunlun Mountains on the north western margin of the Tibetan Plateau (Fig. 1). The Ashikule basin is in a unique tectonic setting, characterized by ongoing strong tectonic activity. In 2008, an earthquake with a magnitude of Mw7.1 occurred on the south side of the basin (Yu et al., 2014). Furthermore, a local newspaper reported that a central volcano in the AVC erupted on May 27, 1951 (Liu and Maimaiti, 1989). The AVC consists of fourteen main volcanoes with dozens of parasitic volcanoes. Wuluke, the volcano of interest in this project, is located in the central eastern part of the volcanic cluster. Due to recent nearby eruptions and tectonic activity, it can be assumed that the Wuluke volcano still has eruption potential. As a result of the remote location and inhospitable weather conditions, relatively little research has been done in the AVC (Yu et al., 2014). Further research within the AVC is needed in order to gain a better understanding of the volcanology and magmatic processes of the northwest Tibet Plateau.

Volcanic rocks in northwestern Tibetan Plateau contain not only information on mantle sources but cryptic signals from the deep crust entrained during magma ascent if mineral xenocrysts are present. Zircon xenocrysts have long been considered burdensome because they can hinder the age estimation of intrusive rocks. However a growing number of studies have shown that xenocrystic zircons can provide valuable information about the deep crust (Liu et al., 2013). Zircon xenocrysts with pre-eruption ages captured

by the magmas could have originated from mantle derived rocks or from assimilation of country rock during the magma's ascent through the crust. Zircon xenocrysts in mantle-derived magmas offer a unique opportunity to study magma evolution by evaluating the role of crustal assimilation. If most xenocrystic zircons can be confirmed as continental crustal zircons (rather than mantle-derived zircons), and if they display multiple age populations, then they may be used to probe deep crustal evolution through time.

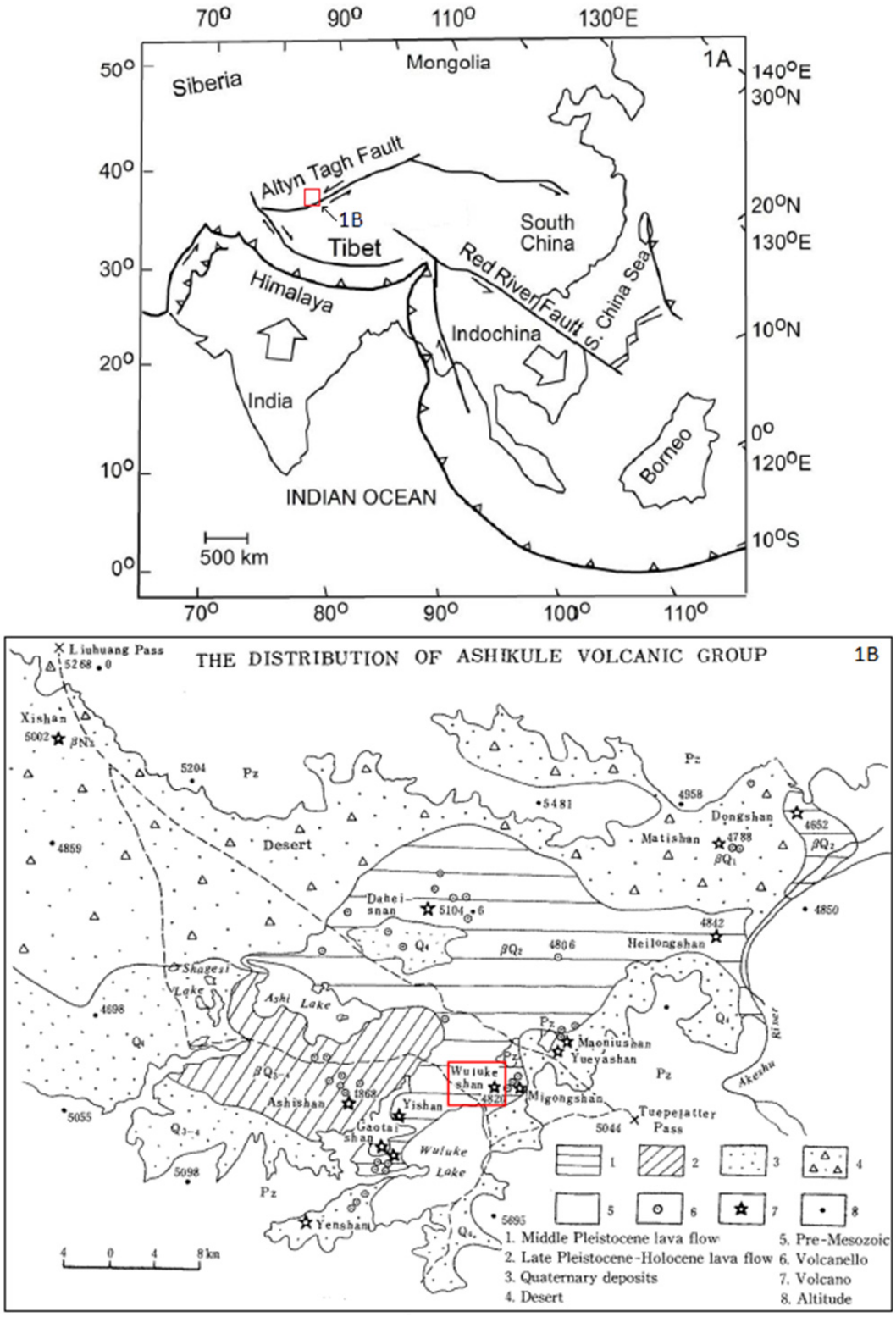

Fig. 1. (A) Regional map showing major tectonic features in Asia. The Ashikule basin is within the red box (Modified from Tapponier et al., 1990). (B) Distribution of Ashikule volcanoes. The Wuluke volcano is within the red box (Modified from Liu and Maimati, 1989).

Zircon U-Pb dating is often referred to as the gold standard of geochronology. When zircon crystallizes, it incorporates U but little Pb (Ireland and Williams, 2003), which makes zircon particularly suitable for U-Pb dating. Secondary ion mass spectrometry (SIMS) provides high spatial resolution (<25 μm) for zircon U-Pb dating using spot analysis of polished zircons. SIMS depth profiling of unpolished zircon surfaces offers even higher spatial resolution (~3 μm).

In this study, ^{238}U-^{206}Pb zircon ages, electron microprobe data of minerals and glasses, and whole-rock major and trace element concentrations are reported for the Wuluke volcano. Zircon inheritance from country rocks is interpreted based on the reported ages. The notable abundance of zircon xenocrysts in the rock sample from the Wuluke volcano provides an excellent opportunity to study magma evolution by comparing age populations of zircons obtained through SIMS.

OBJECTIVES

This research attempts to better constrain the magmatic processes associated with the Wuluke volcano. The comprehensive objective is to obtain age populations from zircon crystals from the Wuluke volcano. The measured age populations, in conjunction with geochemical analysis of the minerals and the whole rock, are used to provide constraints on magma evolution and crustal contamination processes of the Wuluke volcano.

These objectives will be accomplished by (1) age dating of zircon crystals from rocks from the Wuluke volcano using SIMS U-Pb methods, (2) using an electron microprobe to measure mineral and glass major element compositions and determine intensive parameters (temperature and oxygen fugacity fO_2), and lastly (3) characterizing rock type from whole-rock major and trace element analysis using X-Ray fluorescence and ICP-MS, respectively.

BACKGROUND

Geologic Setting

The highly uplifted Tibetan plateau is one of the most spectacular examples of a continental collision event (Chatterjee et al, 2013). The Tibetan plateau is a large upland plateau averaging more than 5 km in elevation. The great height of Tibet is a consequence of underthrusting of India beneath Tibet. The convergence between the Indian and Eurasian plates began in the early Eocene (~50 Ma). This collision resulted in the subsequent northward subduction of the Neo-Tethyan seafloor beneath the southern margin of Asia (Chatterjee et al., 2013). The Indus-Zangbo suture zone defines the area of final collision between the Indian plate and the Tibetan Plateau and marks the zone where the Neo-Tethys ocean was entirely consumed by subduction processes. Thickening of the Tibetan crust to almost double the normal crustal thickness occurred by north-south shortening and vertical stretching during the middle Eocene to early Miocene indentation of Eurasia by India (Dewey et al., 1988).

The Tibetan plateau consists of a number of exotic continental crustal terranes (Fig. 2), between the Himalayas and the Tarim craton, that were successively accreted to Asia prior to its collision with India (Dewey et al., 1988). These terranes were accreted to Asia north of the Indus-Zangbo suture along zones, identified by outcrop belts of ophiolite fragments, which are also interpreted as sutures (Chatterjee et al., 2013). The

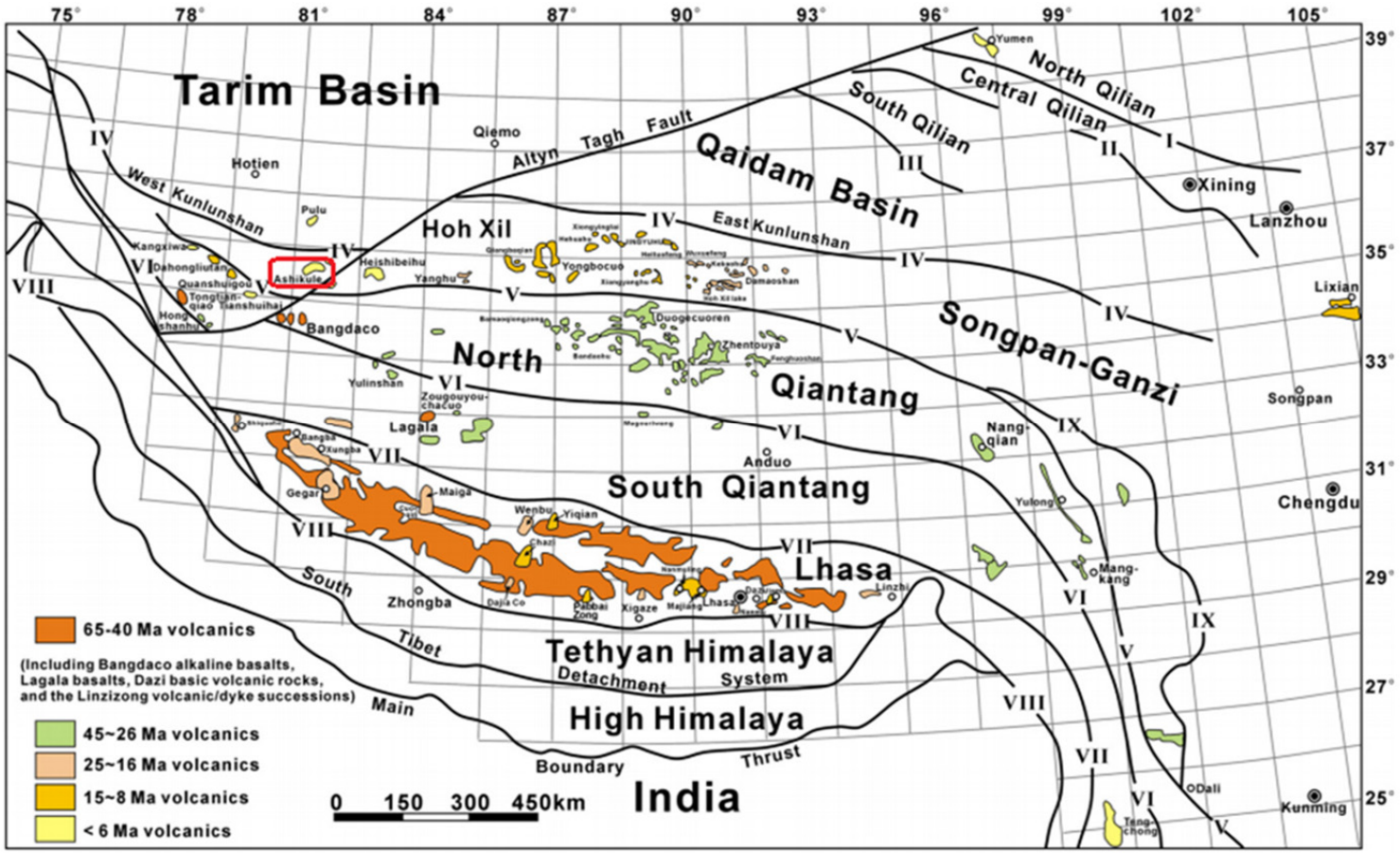

Fig. 2. Simplified map of the Tibetan Plateau showing the distribution of Cenozoic volcanic rocks and the major terranes (Modified from Xia et al., 2011). The Ashikule area is within the red box.

terranes from north to south consist of the Kunlun, Songpan-Ganzi, Qiangtang and the Lhasa terranes.

The Tarim craton is one of the major cratons in central Asia. The Tarim craton represents a rigid region north of the Tibetan plateau able to resist deformation due to its strong Precambrian lithosphere. The Tarim basin is filled with thick Cenozoic sediments (Wang et al., 2003). This strong inhomogeneity resisted deformation resulting from the continuing convergence between the Indian plate into the Eurasian plate. The Tarim craton is separated from the Tibetan plateau by giant transform faults such as the Kunlun and Altyn Tagh faults (Fig. 3) (Dewey et al., 1988). These strike-slip faults accommodate the stress associated with crustal shortening occurring within Tibetan crust (Fig. 4). Sinistral strike-slip movement is associated with the eastward lateral extrusion of the Tibetan plateau, resulting from the continuing indentation of India into Asia (Tapponnier et al., 2001). The Ashikule basin is home to the AVC and is located on the north west edge of the Tibet Plateau on the top of the Western Kunlun Mountains. The Ashikule basin is roughly 700 km^2 in area, surrounded by the Western Kunlun Mountains in the form of a crescent (Cooper et al., 2002). The basin lies in an active extensional tectonic basin at the convergence of the Altun Tagh and Kunlun fault zones. Three salt lakes, Ashikule, Wulukekule and Shagesikule, lie in the center of the basin (Liu and Maimati, 1989). Resting atop the towering Western Kunlun Mountains, the AVC is one of the highest elevation volcanic regions in the world, with an average altitude of 5000 meters. (Yu et al., 2014). The AVC consists of 14 main volcanoes and dozens of parasitic cones. Volcanism has been occurring in the area from the Late Pleistocene to the present. The

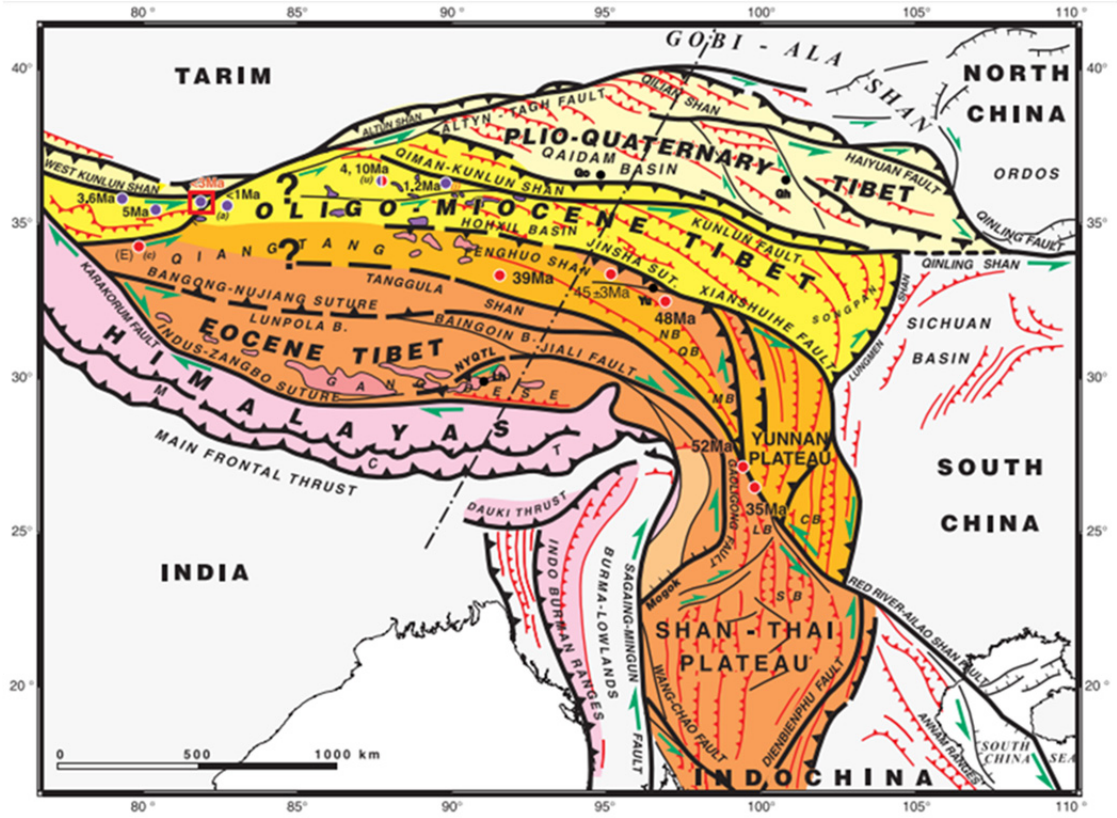

Fig. 3. Major tectonic boundaries and Tertiary faults in Tibet. Bold black lines are major faults and localized shear zones. Dashed where uncertain. Thin red lines are crustal thrusts. Red and violet circles are Eocene and Plio-Quaternary magmatic centers, respectively, in central Tibet. Patches with deep pink and violet shades show other areas with Eocene–Early Miocene and Late Miocene–Quaternary lavas, respectively. Orange to pale yellow shades represent inferred ages of principal plateau-building epochs at expense of Asian crust. Light pink shade south of Zangbo suture and west of Shan plateau indicates thickened Indian crust. Lh, Lhasa. Go, Golmud. Gh, Gonghe. Yu, Yushu. Red square is location of AVC. (Modified from Tapponnier et al., 2001).

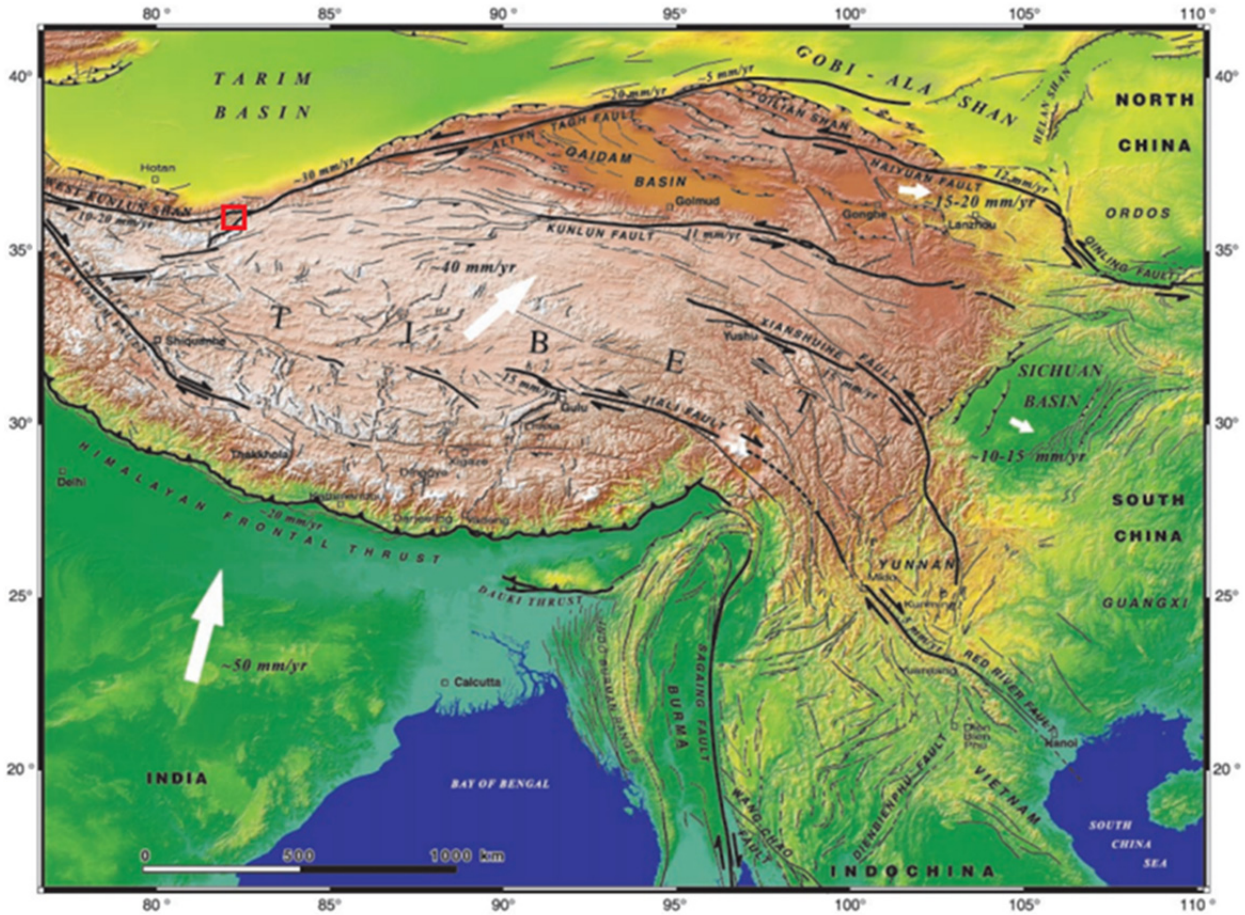

Fig. 4. Topography and principal active faults of Tibet. Bold lines are faults that slip at least 5mm/year. Bold numbers indicate movement rates where known. Thin lines are slower slipping faults. Dashed thin lines are inferred faults. White arrows indicate motions of India, central Tibet, northeasternmost Tibet, and Sichuan relative to Siberia. Red square indicates location of AVC (Modified from Tapponnier et al., 2001).

last volcanic eruption occurred in 1951. The majority of the AVC is covered in lava flows from middle Pleistocene to Holocene. (Liu and Maimati, 1989)

The Wuluke volcano, has often been referred to as volcano number three in early research. Wuluke volcano is located in the central east area of the AVC within the Ashikule basin (Fig. 5). Located northeast of the Wuluke salt lake, it is characterized by a perfect truncated cone with a crater in the form of a sloping dish. Its altitude is about 4730 meters above sea level with a top diameter of 100 meters. The Wuluke volcano is associated with an episode of volcanism which occurred 0.2-0.12 million years ago. During this time, the volcano erupted and formed a cone and large lava plateau (Liu and Maimati, 1989). The volcano is currently covered in late Pleistocene to Holocene lava flows and the structure of the cone reveals three stages of formation. During the first stage a cinder cone was formed with mixing of country rock debris and a gentle outer slope. During the second stage, country rock splashdown was accumulated along the rim. Finally, during the third stage, ropy lava flowed towards the southeast, entering the Wuluke Lake (Xu et al., 2012).

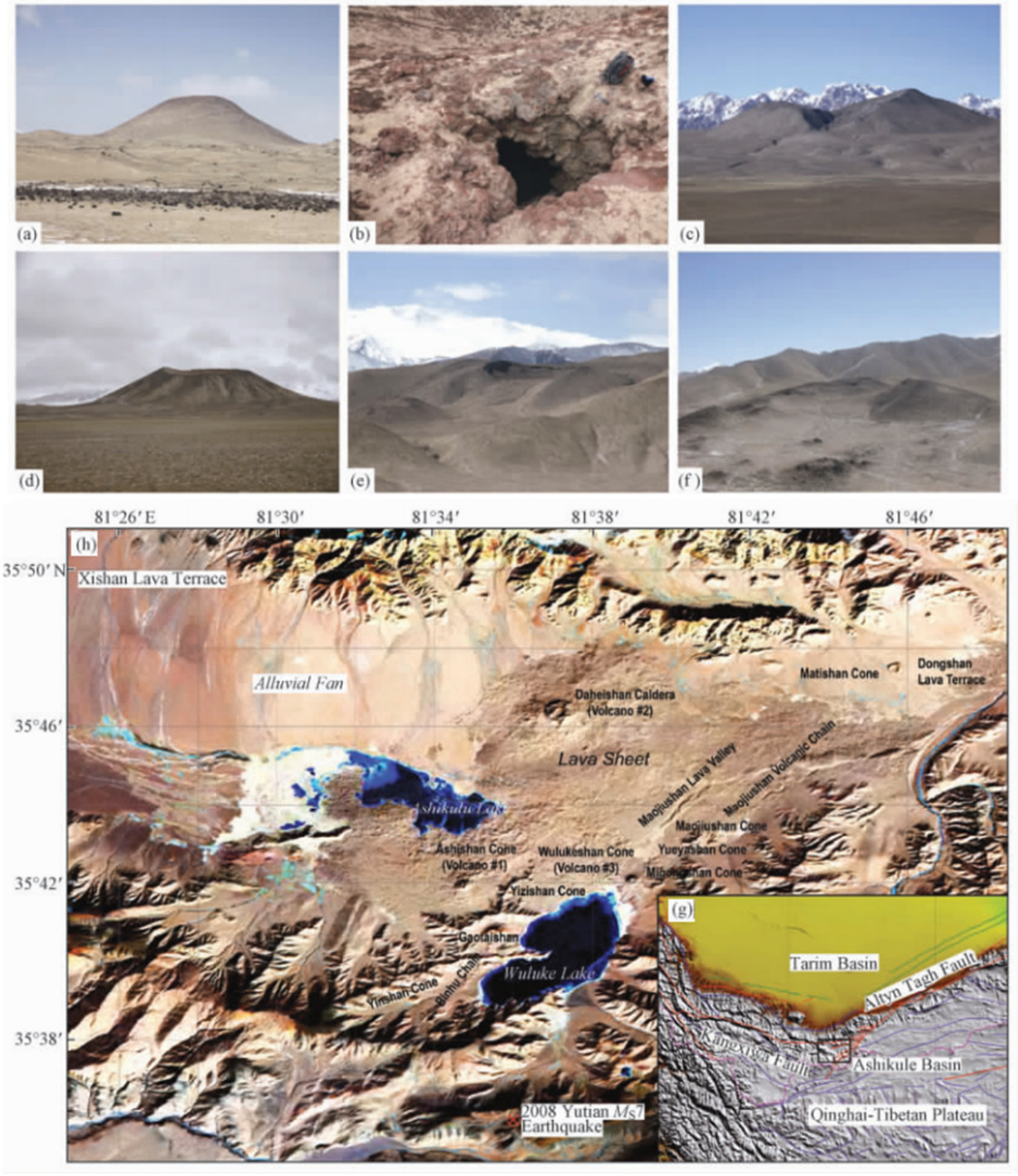

Fig. 5. Characteristic volcano cones and lava terraces of the AVC (A) Ashi volcano; (B) Volcanic gas vent of Ashi; (C) Daheishan volcano; (D) Wuluke volcano; (E) Yizishan volcano; (F) Migongshan volcano. The tectonic location of Ashikule basin (H) and volcano distribution in the basin (G) (Xu et al., 2012).

Concerning Zircons

Zircon ($ZrSiO_4$) is a well-known refractory mineral, capable of enduring metamorphic processes without altering its composition. It is a physically and chemically robust mineral, stable in temperatures up to 1690º C and pressures up to 4.8 GPa (Finch and Hatcher, 2003). This stability in extreme temperatures and pressures allows zircon to survive partial melting of their host rocks. Zircon is a common accessory mineral found in sedimentary, metamorphic, and igneous rocks and are mostly known for their importance in geochronology. This is because during crystallization, zircon incorporates radioactive uranium (U) into its crystal structure, but very little lead (Pb). Over time, the steady decay of U results in the accumulation of radiogenic Pb, providing the basis of for accurate isotopic age dating (Scherer et al., 2007).

Zircons are most common in igneous rocks of intermediate to felsic composition. In extrusive volcanic rocks, zircons tend to crystallize rapidly, resulting in small crystals that typically show an acicular habit (Hoskin and Schaltegger, 2003). Additionally, due to its resilient nature, zircon often preserves an isotopic record of different crystallization events through growth zoning which is a common texture in igneous zircons. Zoning is best revealed with the use of Cathodoluminescence (CL) imaging of polished grains (Ireland and Williams, 2003).

Zircon is one of the most versatile and most commonly used geochronometers available and thus has played a key role in crustal evolution studies (Scherer et al., 2007). This current study will focus on the occurrence of zircons found in young igneous rocks and will attempt to use zircons to investigate deep crustal evolution and identify if contamination has occurred. Dating of zircons from igneous rocks will yield the age at

which the host rock cooled from a melt. Xenocrystic zircons, also referred to as inherited zircons, are not derived from their host rock and instead were crystallized from a different magma. Consequently, it can be concluded that xenocrystic zircons are older than their host rock and the associated phenocryst zircons. Zircon xenocrysts are often an indication that the magma of the host rock experienced contamination. If significantly older age populations of zircons exist within the host rock, it would suggest crustal contamination through magma mixing or the assimilation of country rock. If most xenocrystic zircons can be confirmed as continental crustal zircons, and if they display multiple age populations, then they may be used to examine deep crustal evolution through time.

U-Pb Decay Series

Radiometric dating is the process of determining the age of rocks based on the decay of their radioactive isotopes. This technique uses the principle that radioactive parent isotopes decay at constant rates through time into daughter isotopes. These regular intervals of decay are called half-lives. The half-life of a decay pair is the time it takes for half of the parent isotope to decay into a daughter isotope. The rate of decay, also known as the decay constant, is essentially the probability of decay per unit time (Zou, 2007). The decay constant is specific to each radioactive isotope and is not influenced by outside factors such as pressure or temperature. The constant rate of decays allows geologists to use radiometric dating as a natural clock for determining the numerical age of a rock. Some minerals however may incorporate daughter isotopes into the initial composition. In this case, a correction needs to be performed to remove the initial daughter isotopes from the age calculation. Zircon, however, includes little to no initial Pb during its

formation, providing the basis for accurate and precise isotopic age determination (Sherer et al, 2007).

Uranium-series dating is one of the most common isotopic series in radiometric dating. This is because it provides several intermediate isotopes before reaching the final stable ^{206}Pb isotope (Fig. 6). This provides a wide range of time frames useful for dating. For example, ^{238}U-^{230}Th has a half-life of 75,690 years, while ^{238}U-^{206}Pb has a half-life of 4.5 billion years (Tucker, 2011). Additionally, since most accessory minerals exclude Pb from formation, ages based on U-Pb decay pair are widely accepted.

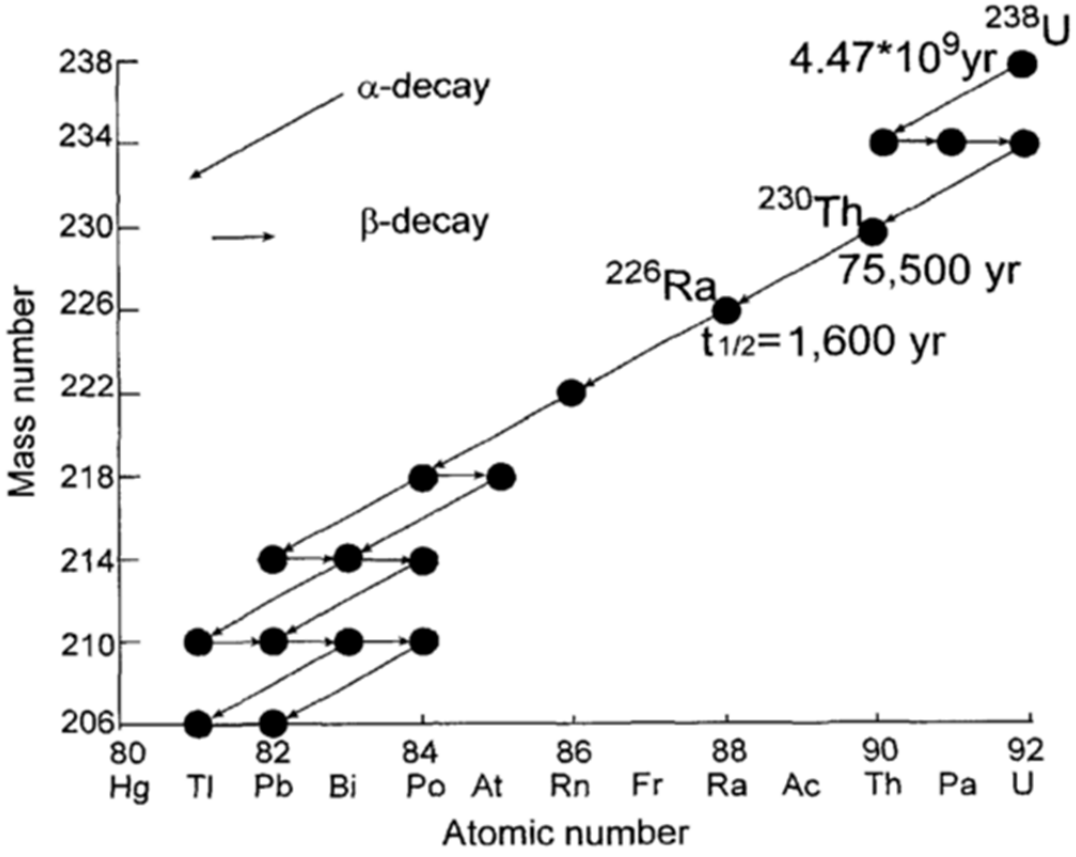

Fig. 6. Decay series of ^{238}U to the final stable ^{206}Pb showing intermediate isotopes ^{230}Th and ^{226}Ra, $t_{1/2}$ denotes half life (Zou et al., 2007).

Secondary Ion Mass Spectrometry (SIMS)

Secondary ion mass spectrometry (SIMS) is a versatile radiometric dating technique used to measure the composition of solid materials on a micron scale. SIMS is most commonly performed using an ion microprobe, which uses a focused negative primary ion beam generated in a duoplasmatron (Ireland and Williams et al., 2003). SIMS dating works by sputtering the sample with a primary ion beam of $^{16}O^-$ ions at sputter rates of ~0.05μm/nA/sec (Zou et al., 2010b; Tucket et al., 2013). After sputtering the sample with a primary beam of $^{16}O^-$ ions, a small percentage of atoms will become ionized. These secondary ions are then accelerated in the mass spectrometer where they are measured and counted (Fig. 7). Used in conjunction with surface imaging techniques such as backscattered electron and cathodoluminescence, SIMS can finely target specific areas on the exposed crystal surface for isotopic analysis.

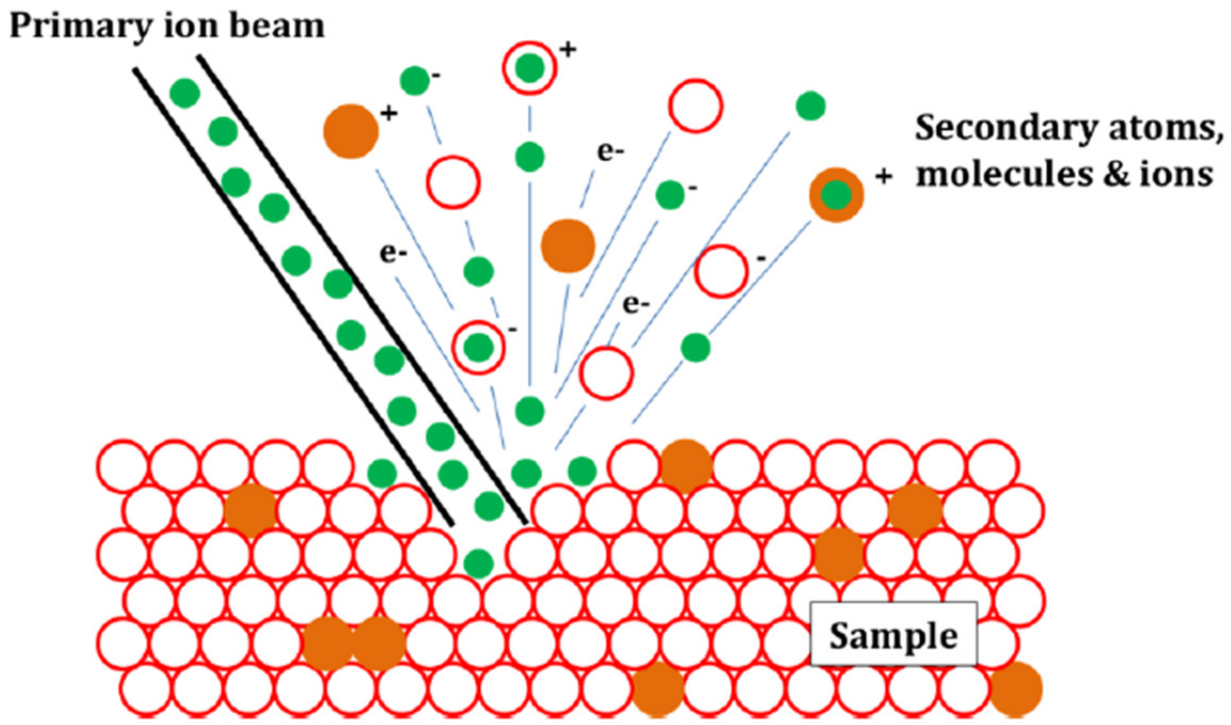

Fig. 7. Diagram depicting a sample being sputtered by a beam of primary ions, resulting in the backscatter of secondary atoms, molecules, and ions (Tucker, 2011).

Certain precautions must be taken to ensure the SIMS does not record erroneous data, which could be due to any number of different instrumental and sample preparation errors. To make certain these errors are not occurring, multiple zircon standards are mounted along with the unknown zircon samples. Standards are zircons with known ages. By using SIMS on these standards, one can determine if there is an error with the machine and thus make the necessary adjustments before proceeding with the sample zircons. Even though zircon incorporates minute amounts of Pb at the time of crystallization, the presence of common Pb must be estimated if an accurate age is to be accurate. Common Pb in a zircon can originate from many sources including microscopic mineral inclusions, Pb added to the zircon during or after alteration, laboratory Pb from polishing compounds, and coating materials. The following equations shows how common Pb content can be estimated (Zou, 2007).

$$f = {}^{206}Pb_{\ init} / {}^{206}Pb_{\ tot}$$

Next *f* can then be calculated as,

$$f = \frac{({}^{204}Pb/{}^{206}Pb)_{\ tot}}{({}^{204}Pb/{}^{206}Pb)_{\ init}}$$

SIMS has many advantages over other radiometric dating techniques. Total sampling depth is typically less than 5um with a target area usually 10 to 50 um in diameter (Ireland and Williams, 2003). SIMS is effectively the least destructive compared to other dating techniques such as Laser Ablation Inductively Coupled Plasma Mass Spectrometry (LA-ICPMS) and Thermal Ionization Mass Spectrometry (TIMS) (Fig. 8). There is also very little heating and vaporization due to a much lower amount of energy absorbed by the target (Stern, 2009). Depending on how well the mount is cleaned after polishing and the Pb content of the Au coat, it is possible to measure radiogenic Pb

contents down to a few ppb and therefore measure the Pb/U age of zircon as young as a few hundred thousand years. These statistics can be further improved by longer counting times and targeting zircon zones that are U-rich. Although SIMS analysis does not achieve the precision attainable with TIMS because of the small volume of material sampled, it has a particular advantage with its precision and accuracy in U-Th-Pb dating at an intra-crystalline scale (Ireland and Williams, 2003).

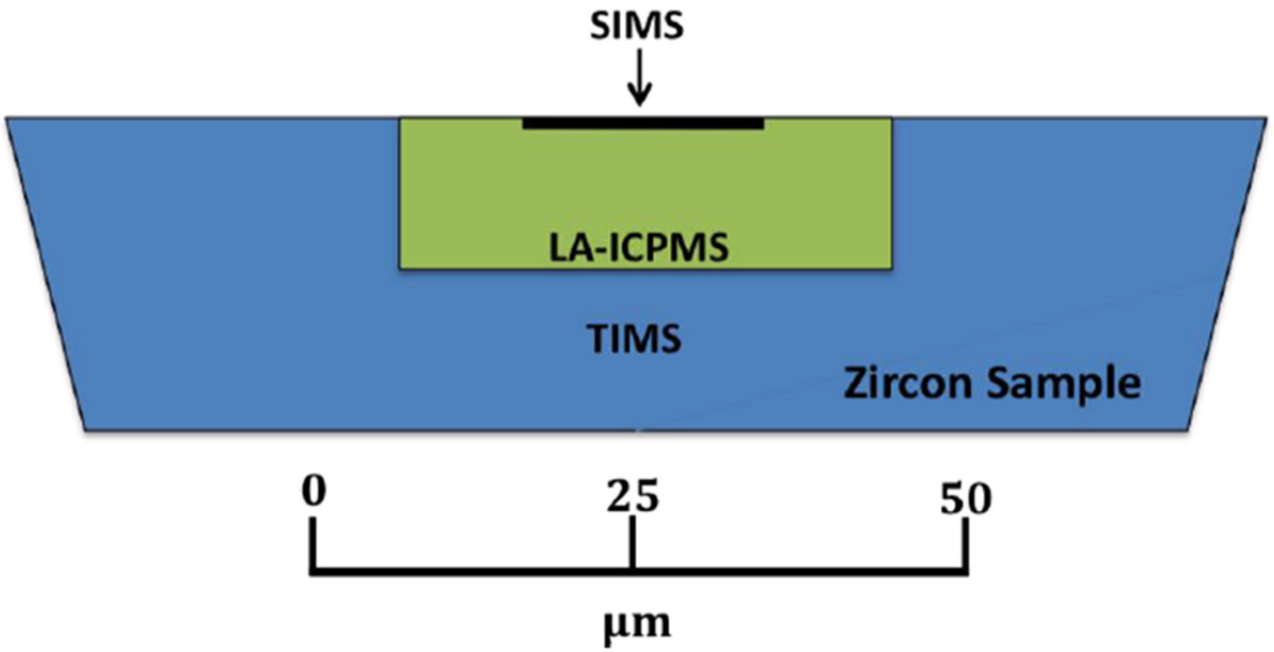

Fig. 8. Diagram depicting average zircon sample destruction area of SIMS, LA-ICPMS, and TIMS in cross-section view. SIMS spot size is typically 10-20 µm and <2 µm depth. LA-ICPMS spot size is typically 30-60 µm and 10-20 µm depth. TIMS analysis entirely consumes the sample (Košler and Sylvester, 2003).

PREVIOUS WORK

Not much research has been done on the AVC and very little has been focused solely on the magmatism associated with the Wuluke volcano. Due to the difficulty of access, the AVC located in the towering West Kunlun Mountains is a poorly documented region in China. The earliest geological research within the AVC was some reconnaissance field work to conduct an investigation of the volcanic field after reports of volcanic activity. During the fieldwork, geologists found four volcanoes and called them number one, two, three and four (Zhao, 1976). The Wuluke volcano was referred to as number three until additional field work uncovered many more volcanoes and parasitic volcanoes in the field.

The earliest radiometric dating of these volcanoes was K-Ar dating performed by Liu and Maimati (1989). The dating revealed three main episodes of volcanism in the AVC (Table 1). This included an episode during early middle Pleistocene (0.67-0.5 Ma), a second episode occurring in the middle Pleistocene (0.44-0.28 Ma) and the third episode, also called the Wuluke episode, occurred during the late middle Pleistocene (0.2-0.12 Ma) (Liu and Maimati, 1989). During the third episode the Wuluke volcano erupted and formed a cone.

Table 1.
K-Ar dating of Ashikile Volcanoes (Liu and Maimati, 1989).

No.	Place	Latitude (N)	Longitude (E)	Weight (g)	K%	40Ar* E-12 moles/g	40Ar* %	age & error (Ma)	
K713	Migongshan	35°41′58″	81°39′45″	11.8016	3.07	2.2432	1.94	0.42±0.01	0.44±0.01
						2.4077	1.93	0.45±0.01	
K716	Wulukeshan	35°42′	81°39′	10.0067	3.44	1.1797	3.67	0.20±0.05	
K718	Volcanello near Migongshan	35°42′	81°39′40″	10.0448	3.48	1.7706	12.37	0.29±0.01	0.28±0.01
						1.7151	11.71	0.28±0.01	
K720	Heilongshan	35°45′17″	81°41′40″	10.9389	3.07	3.6435	4.55	0.68±0.01	0.67±0.01
						3.5110	4.41	0.66±0.01	
K721	Matishan	35°47′26″	81°45′40″	10.0487	3.12	8.9242	10.63	1.65±0.16	
K723	Dongshan	35°48′17″	81°48′	10.7627	2.99	2.7367	5.08	0.53±0.01	0.52±0.01
						2.6532	4.96	0.51±0.01	
K729	Yishan	35°41′25″	81°36′12″	11.3912	3.60	3.6962	2.36	0.59±0.01	0.58±0.01
						3.5576	2.31	0.57±0.01	
K732	Yueyashan	35°42′45″	81°40′53″	10.2983	3.48	1.8873	1.42	0.31±0.01	
K736	Daheishan (mid.)	35°46′15″	81°37′	8.6592	2.92	3.0904	19.73	0.61±0.01	0.60±0.01
						3.0451	19.54	0.60±0.01	
K738	Daheishan (top)	35°46′ 5″	81°36′30″	8.0032	2.88	2.5029	3.88	0.50±0.13	
K740	West lava of Ashishan	35°42′	81°30′	16.7597	3.82	0.7697	3.02	0.12±0.002	0.12±0.002
						0.8260	3.11	0.12±0.002	
K743	Xishan	35°50′39″	81°26′30″	8.0082	3.73	18.1133	50.0	2.80±0.06	
U601	Kangulake lava (upper)			5.9960	3.54	7.3038	24.19	1.19±0.02	1.19±0.02
						7.2767	24.13	1.19±0.02	
U606	〃			5.1629	3.69	7.8539	27.36	1.23±0.04	
U604	Kangulake lave (lower)			6.0762	3.46	8.5719	49.84	1.43±0.03	

Note: ＊Radiogenic argon, (1) All samples are whole rock of trachyandesite, (2) potassium analysis by flame meter, and argon measured by RGA spectrometer, (3) Constants: $\lambda e = 0.581$ E-10year^{-1}, $\lambda\beta = 4.962$ E-10year^{-1}, 40k/k = 1.167 E-4 (atoms)

Based on statistical and analytical data on more than 170 isotopic ages and the characteristics of magmatism and other tectonic activity in the region, five stages of tectono-magmatic evolution have been distinguished in the Western Kunlun Orogen. (Bi et al., 1999). The first stage occurred between the late Archean (~2700 Ma) and early Middle Proterozoic (~1400 Ma). During this stage, the Western Kunlun Orogen was in the developing stage of the active continental margin. There is no isotopic age evidence for magmatic activity during the second stage, however there is a time gap between 1400 Ma and 1000 Ma. This time gap demonstrates that the magmatic activity had subsided. The third stage is divided into two sub stages. The former stage isotopic ages range from ~977 Ma to ~651 Ma. This stage is represented by ultra-basic and basic volcanic eruptions controlled by regional faults. The later stage isotopic ages ranges from ~644 Ma to ~255 Ma with magmatism characterized by the intrusion of acidic magmas. Again, no isotopic age data has been found within a 20 Ma time gap between ~250 Ma and ~230 Ma, indicating weak magmatic activities during the fourth stage. The fifth stage of the tectono-magmatic evolution is the most active stage, with isotopic age data in the range of ~225 Ma to the present. The dominant tectono-magmatic events include the subductions of the Paleo-Tethys and the Neo-Tethys oceans and the subsequent collision of the Indian and Eurasian plates (Bi et al., 1999).

Very little research has been performed in the AVC and the majority of that research has been focused on the recently active Ashi volcano. Geochemical analyses were performed by Yu et al, (2014) on the Ashi volcano, often referred to as the number one volcano in early research (Zhao, 1976). Geochemical analyses revealed that the

magma was derived from crustal- or mantle-derived magma contaminated on its ascent through the crust. Bulk rock geochemistry of the Ashi volcano rocks was analyzed using X-ray fluorescence spectrometry. The rocks generally fell into the trachyandesite field. Phenocrysts in the rocks consist mainly of plagioclase and pyroxene and their chemical compositions were analyzed by using an electron microprobe. The electron microprobe analyses revealed the existence of acidic plagioclases and pyroxenes. Pyroxenes were characterized by low Mg and high Fe content and the plagioclases were characterized by a low An value. Yu et al, (2014) determined that these phenocrysts are not in equilibrium with the trachyandesite magma and inferred that they came from a more acidic magma. It is likely that there are two magma pockets beneath the Ashi volcano. The deeper trachyandesite magma is thought to mix with the acidic magma on its ascent through the crust.

Recent research using zircon geochronology to determine crustal contamination was performed on samples from outside the AVC in the Southern Tibetan plateau from the Lhasa Terrane by Liu et al., (2013). Zircon ^{238}U-^{206}Pb dating and trace element analyses were performed synchronously by using LA-ICP-MS. The sampled zircons defined three major age peaks. Zircons with pre-eruption ages have been identified from mantle derived rocks. Mantle zircons were further identified on trace element signatures. However, the majority of the zircons are not mantle derived and have continental-like isotopic signatures that indicate a xenocrystic origin during magma ascent through the crust. Liu et al, (2013) proposes that zircon xenocrysts with varying ^{238}U-^{206}Pb ages and supporting geochemical data confirm the role of crustal contamination through the assimilation of Lhasa terrane crust.

MATERIALS AND METHODS

Sample Preparation

For this study, a single rock sample (WLK-2B) was previously collected from the Wuluke volcano during a Chinese field expedition. Sample WLK-2B was collected from the lava flow along the northern east edge of the Wuluke volcanic cone. Figure 9A shows an image of WLK-2B and the location from where it was collected along the flank of the volcano.

In order to perform SIMS analysis, whole-rock major and trace element analysis, and to create thin sections to be used with the electron microprobe, the sample had to but cut into smaller pieces. The sample was cut with a compound miter saw at Auburn University. A sample piece was then sent to Langfang Geological Service Company in China to have the zircons extracted. A sample piece was sent to Washington State University Geoanalytical Lab to have x-ray fluorescence (XRF) and inductively coupled plasma mass spectrometry (ICP-MS) combined analyses. Lastly, several sample pieces were sent to Wagner Petrographic to have thin sections made for analysis with an electron microprobe.

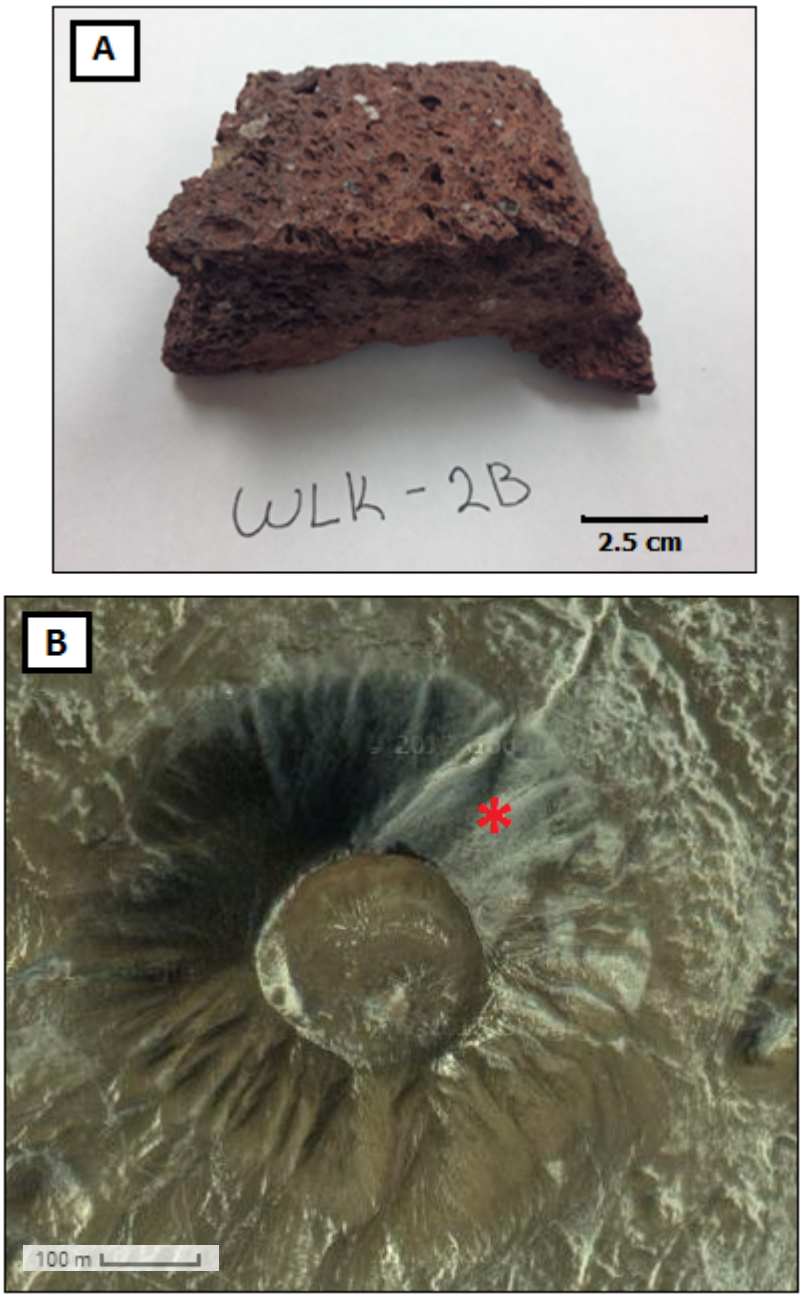

Fig. 9. (A) Sample that was collected from Wuluke volcano. (B) Location of sample collection on Wuluke volcano (From Google Earth).

U-Pb Dating

After the zircons have been extracted, they must be specifically prepared and mounted for SIMS analysis. This work was performed in the laboratory facilities at the University of California, Los Angeles (UCLA) by the author. The instrument used for SIMS dating was the Cameca ims 1270 at the NSF National Ion Microprobe Facility at UCLA.

1. Sample Preparation

After the zircons have been extracted, they must be specifically prepared, and mounted for SIMS. Secondary ion yields are sensitive to local topographic and electrostatic features of the sample mount (Stern, 2009) thus proper sample preparation is of the utmost importance for SIMS. Using a fine-point needle, zircon grains are carefully selected and placed onto a piece of double sided tape. Roughly 80 zircon grains were placed in rows on the double sided sticky tape along with approximately 20 standard zircon grains. Next, a Teflon mold measuring 2.5cm diameter was placed around the perimeter of the grains, and an epoxy mixture was poured into the mold. The epoxy was allowed to dry overnight. The following morning, the tape was slowly removed from the sample and the mold was removed by using a hand crank. The hardened epoxy was then shaved down to an appropriate thickness (~.63 cm). The sample was then polished to ensure the zircon grain surfaces were exposed and flat. The sample was gently polished using 1200 grit silicon carbide paper for 30 minutes in 30 second intervals.

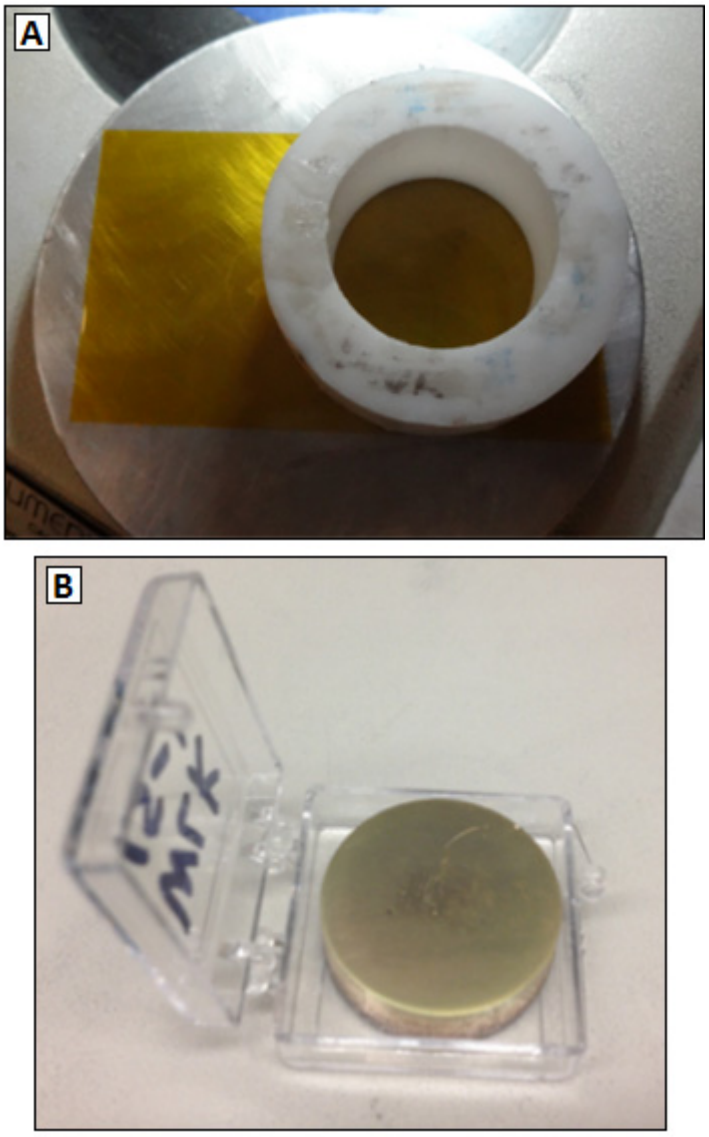

Fig. 10. (A) Close up image of Teflon mold over double sided sticky tape. (B) Image showing final mount covered in thin gold layer.

After the mount had been prepared, it was placed into a scanning electron microscope and CL and BSE images were taken of the zircons (Fig. 11). Lastly, the epoxy mount was washed with soapy water, dilute HCL, methanol, and then dried in an oven. The cleaned and dried mount was plated in a gold coater to achieve a thin 20-40 nm gold layer to generate a conducting surface. Next the mount was placed into the sample holder which has a ~2.5cm diameter (Fig. 12). The sample holder must then be inserted into the Cameca ims 1270 through an airlock system because the ion probe is kept under ultra-high vacuum (UHV). The sample was then sputtered with a primary beam of O^{16-} ions generated in the duoplasmatron in order to obtain U-Pb ages from each zircon. The duoplasmatron works by converting gas into negative primary ions which is then focused into an ion beam. Zircon sputter rates are ~0.05 μm^3/nA/sec and the typical time required to sputter one zircon is ~20 minutes (Zou et al., 2010b). After the SIMS analysis was completed, the mount containing the polished zircons with SIMS craters was kept for potential future analysis.

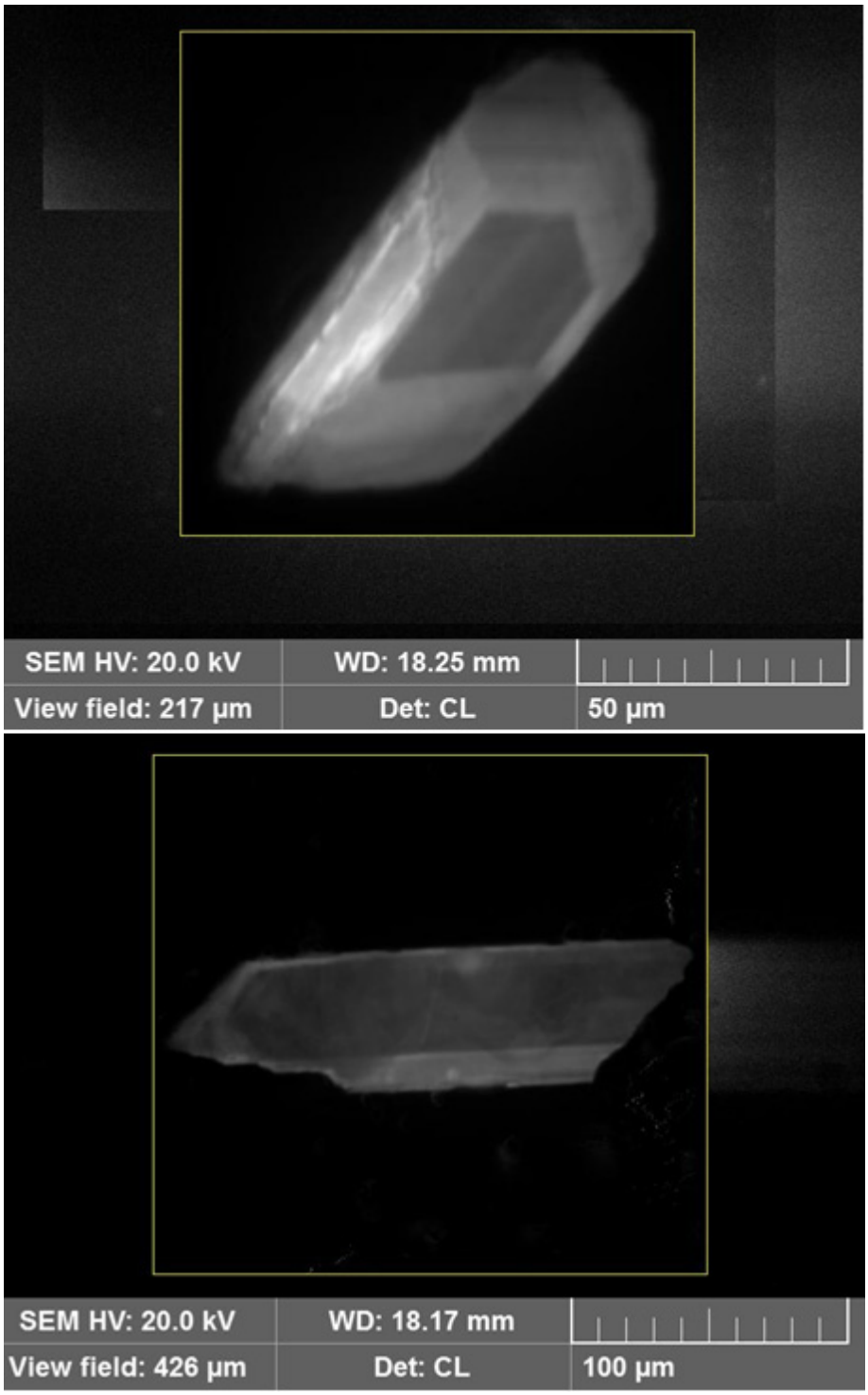

Fig. 11. CL images of zircons from mount, before thin gold coat.

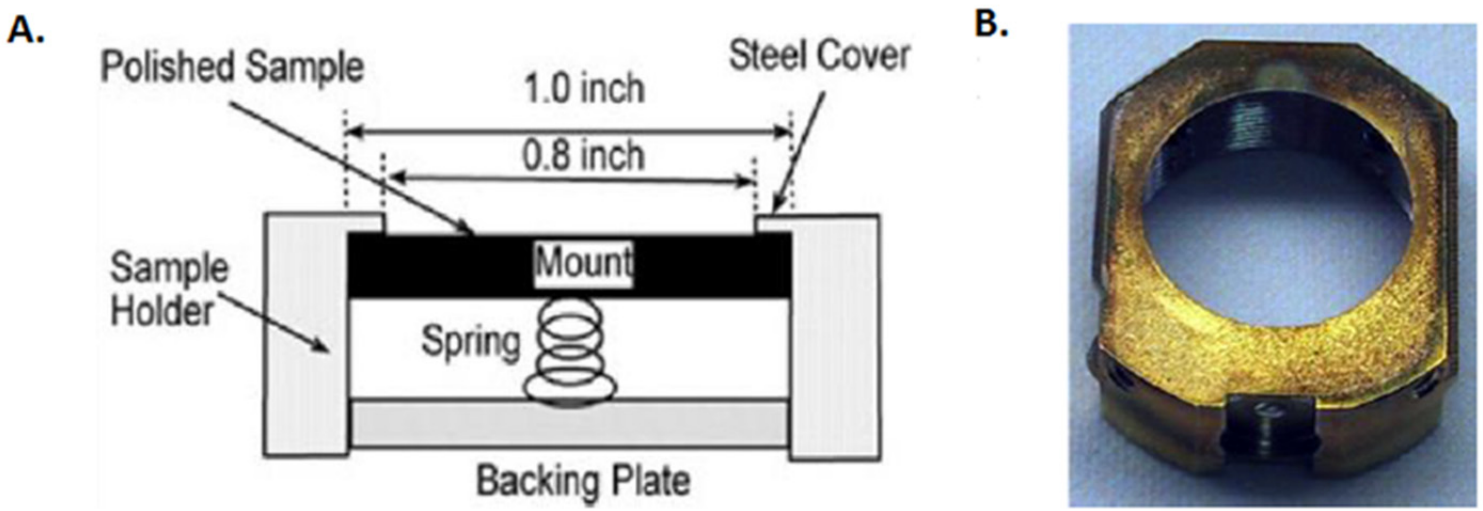

Fig. 12. (A.) Schematic diagram of a sample holder showing the backing plate and spring. Note that the amount of mount surface area available for analysis is decreased by 0.2 inches after insertion into the sample holder. (B.) Photograph of a standard sample holder (UCLA, 2015).

2. Mass Spectrometer

The NSF National Ion Microprobe Facility at UCLA (Fig. 13) was commissioned as a national facility in 1996, and scientists have generated over 300 publications using UCLA SIMS data (UCLA, 2015). U-Pb dating with the Cameca ims 1270 achieves an average precision and accuracy of ~1-2 % (Zou et al., 2010b). This paper addresses the operational procedures for the Cameca ims 1270. Figure 14 represents a 3D schematic of the Cameca ims 1270.

The analysis cycle for zircon U-Pb dating include the Pb isotopes ^{204}Pb, ^{206}Pb, ^{207}Pb, and ^{208}Pb, two of the U and U oxide species and a Th species. Oxides are measured because they typically show higher intensities than metals (Ireland & Williams, 2003). $^{90}Zr_2{}^{16}O_4{}^{+}$ is also measured as a reference. At least two U species must be measured in order to calculate the try Pb/U. The raw data for measured Wuluke zircons are presented in Table 6. AS-3 zircons from the Duluth Complex were used as standards for calibration of the instrument. The primary current was generated at ~30 nA, and the secondary ions were analyzed at a mass resolving power of ~5000.

SIMS works by sputtering a sample with a primary beam of $^{16}O^{-}$ ions. This beam is generated using a duoplasmatron, which converts the gas into a concentrated beam of negative primary ions. The ion beam then travels through the primary ion column before contacting the target sample. After sputtering the sample with the ion beam, a small percentage of the atoms become ionized (typically < 10%) (Stern, 2009). These ionized secondary ions then pass through the secondary ion column into the mass spectrometer containing an electrostatic analyzer (ESA) and an electromagnet. The ESA is used to deflect ions based on their energy levels, while the electromagnet deflects particles based

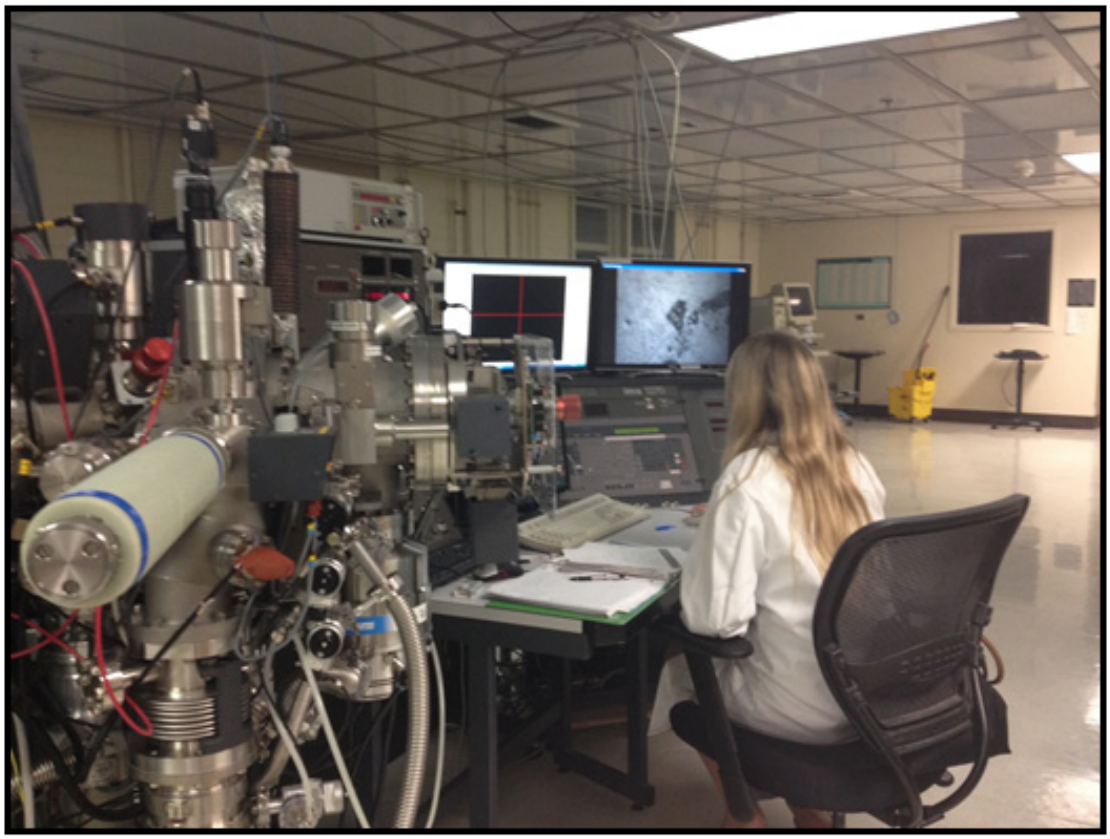

Fig. 13. Photograph of the Cameca ims 1270 at the NSF National Ion Microprobe Facility at UCLA with the author at the control console of the Cameca ims 1270.

on their masses. The last step is to collect and count the secondary ions. Several different secondary ion detection measures may be used according to need including an ion counting electron multiplier, Faraday cups, and ion image detectors (Tucker, 2011). Figure 14 is a simplified diagram showing these fundamental components of SIMS.

Customizable Ion Probe Software (CIPS) allows the components of SIMS to be monitored and adjusted (Tucker, 2011). Individual spots on zircons can also be targeted manually using a magnified view of the zircon surface. After selecting individual spots on the zircon samples, the location of each spot is saved and the zircons are sputtered in series, with each zircon taking ~20 minutes to analyze. Once the sputtering process is complete, the raw data obtained is transferred into another computer for data reduction using a software called ZIPS.

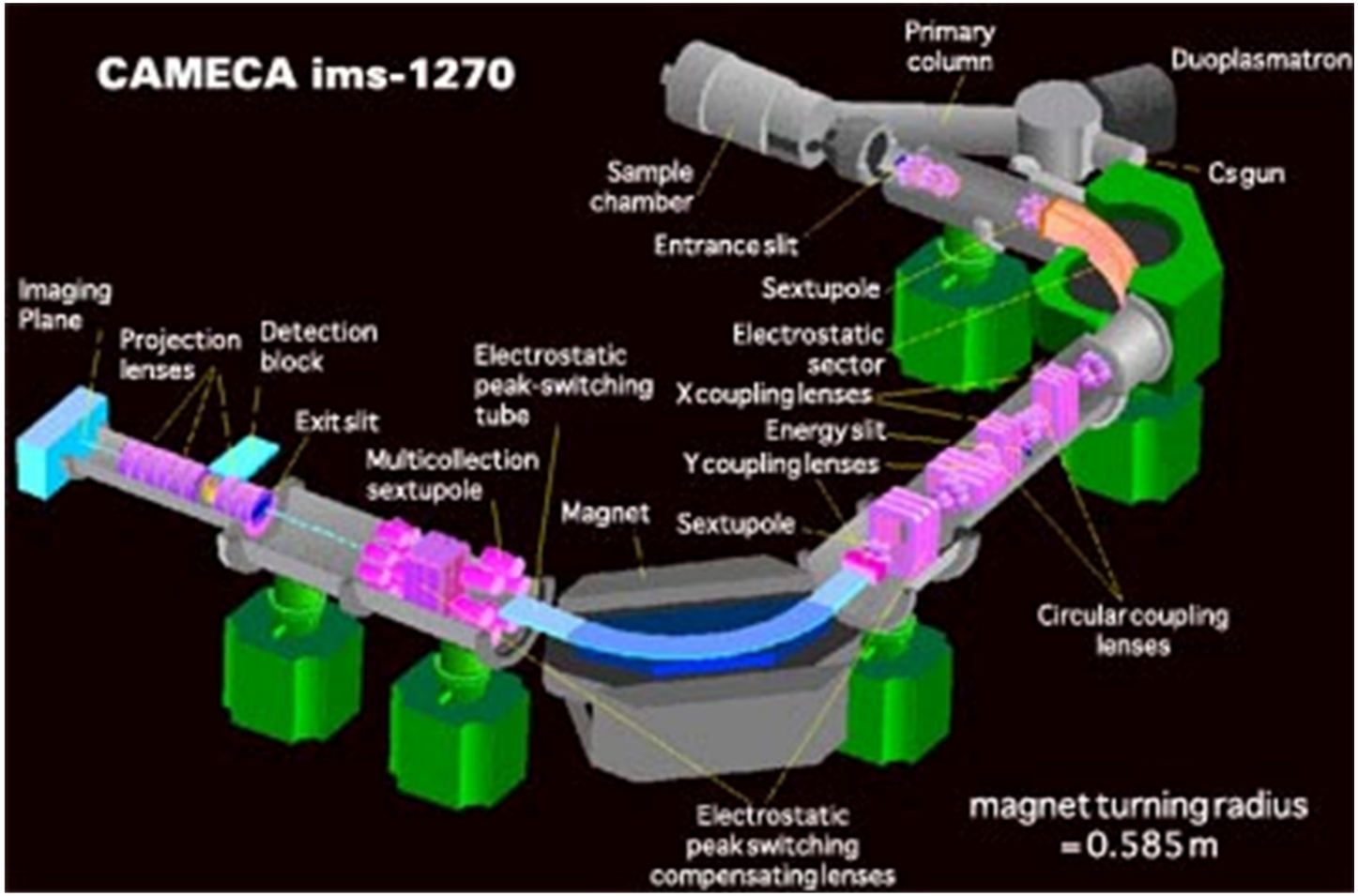

Fig 14. Schematic of the CAMECA ims 1270 ion microprobe in single collector mode (UCLA, 2015).

Electron Microprobe

A total of two polished thin sections from sample WLK-2B were produced by Wagner Petrographic. Before analyzing mineral compositions with the electron microprobe, the thin sections were first observed under an optical microscope to identify all the minerals and locate any possible glass. Fig. 15 shows photomicrographs of the polished thin section.

1. Sample Preparation

Sample preparation was then performed by the author at the University of Georgia Department of Geology Microprobe Lab. The thin sections obtained from Wagner Petrographic were first cleaned using detergent to remove fingerprints and possible accumulated oils that might interfere with the beam. Next the thin sections were placed in a carbon vacuum evaporator to coat the samples with carbon to create an electrically conductive surface and prevent charging. After the thin sections had been successfully coated with carbon they are placed into a sample holder. The sample holder was then inserted into the instrument to analyze mineral compositions.

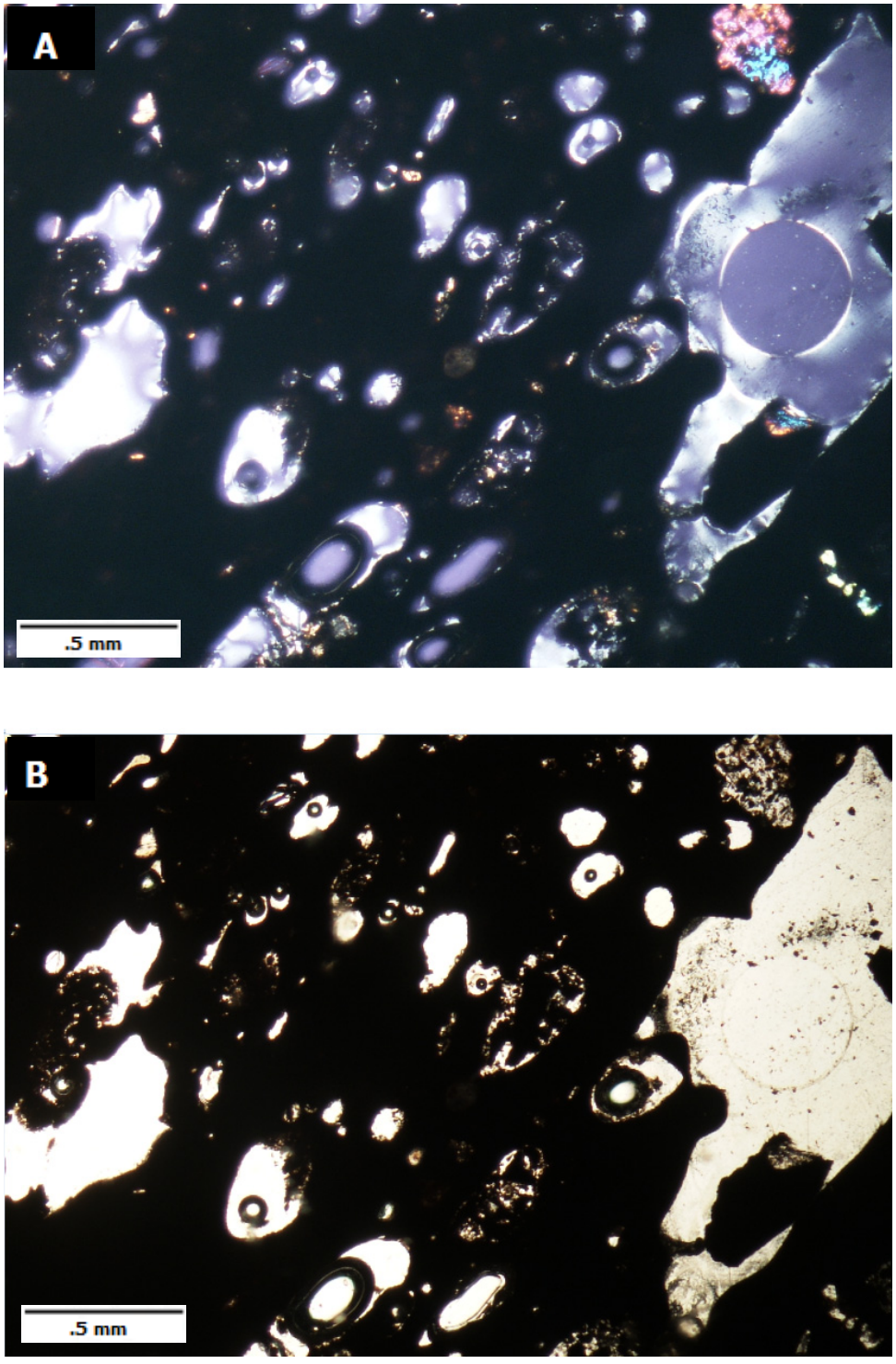

Fig. 15. Photomicrographs of WLK-2B showing vesicles and glass. (A) 2x view with cross polarized light. (B) 2x view with plane light.

2. Microprobe Analyses

Thin sections were analyzed using the JEOL 8600 electron microprobe (Fig. 16) using a 15KV accelerating voltage and 10nA beam current. Mineral grains were qualitatively identified using a Bruker 5010 Silicon Drift Detector (SDD) energy dispersive x–ray (EDS) detector controlled by a Bruker Quantax energy dispersive analysis system. Quantitative analyses were performed with wavelength dispersive spectrometers (WDS) automated with Advanced Microbeam, Inc. electronics and Probe for EPMA software, using 10 second counting times, and natural and synthetic mineral standards. Analyses were calculated using Armstrong's (1988) Phi-Rho-Z matrix correction model.

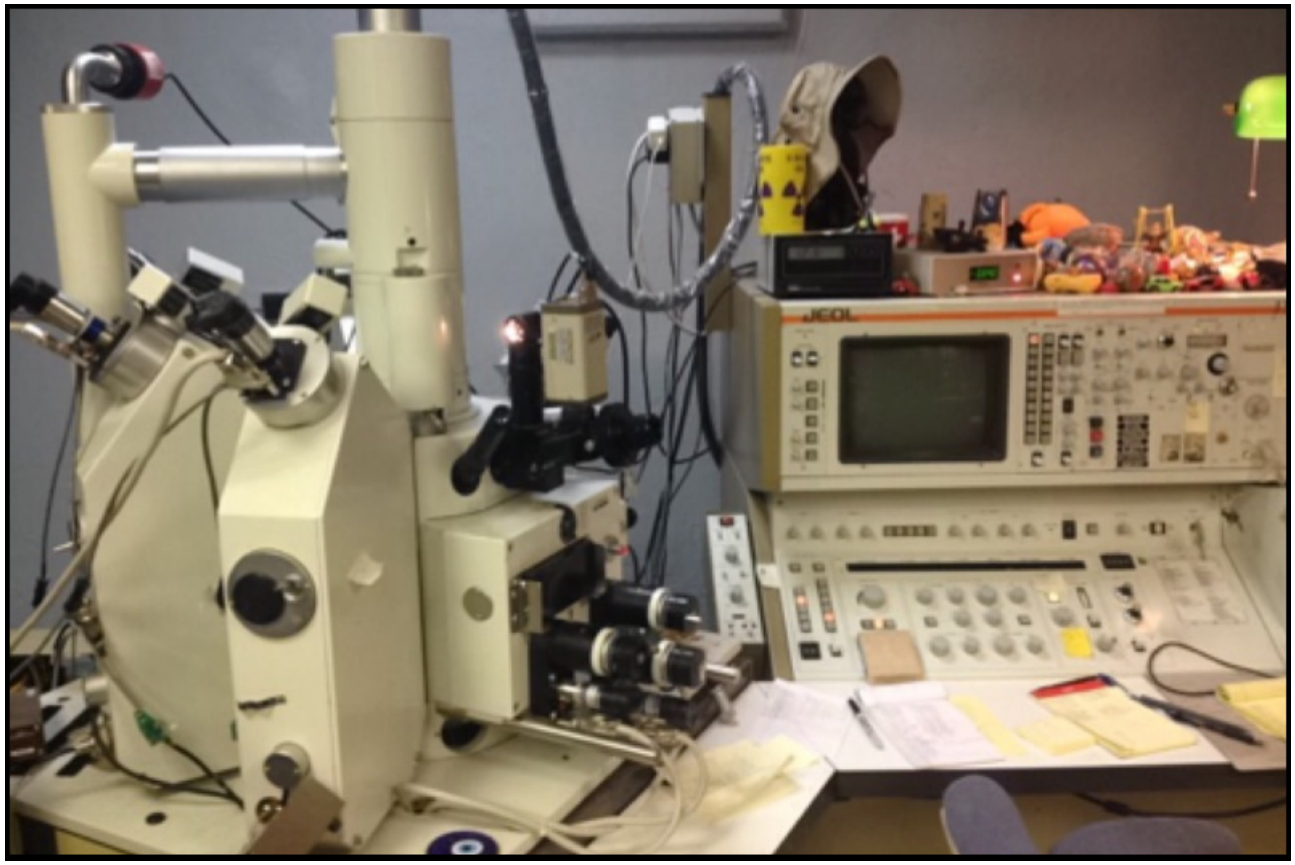

Fig. 16. JEOL 8600 electron microprobe at University of Georgia Department of Geology Microprobe Lab.

RESULTS

Whole-Rock Major and Trace Element Analysis

Major, trace and rare earth element (REE) concentrations from whole rock analysis of WLK-2B can be seen in Table 2. The SiO_2 and K_2O weight percentages of the Wuluke sample were plotted on a K_2O versus SiO_2 plot, and they plot in the shoshonite field (Fig. 17). Shoshonitic rocks have high K-enrichment compared to calc-alkaline and tholeiitic rocks. Shoshonites are uncommon and are found in a few subduction zones overlain by thick continental crust and some island arcs (Best, 2003). The K_2O versus Na_2O plot (Fig. 17) also indicates that WLK-2B is not an ultrapotassic rock.

Whole rock major element concentrations from WLK-2B were plotted on a total alkali silica (TAS) diagram (Fig.18). Results indicate that the Wuluke sample is a trachy-andesite in composition, similar to the whole-rock analysis of rocks from the Ashi volcano (Yu et al., 2014). Additionally, the Wuluke rock sample is peraluminous, with an alumina saturation index (ASI) molecular ratio ($Al_2O_3/(CaO+K_2O+Na_2O)$ of 1.04 and $Al_2O_3/(K_2O+Na_2O)$ of 1.96. Peraluminous rocks are defined as having molecular Al_2O_3 greater than ($CaO+K_2O+Na_2O$). In peraluminous rocks, the excess of alumina is accommodated in mafic minerals. A peraluminous composition, coupled with high Zr concentrations, would most likely stabilize entrained zircon xenocrysts if they were present (Zou et al., 2010a).

Table 2
Whole-rock major and trace element concentrations in WLK-2B.

	wt%		ppm		ppm		ppm
SiO_2	56.33	La	163.3	Er	2.4	U	6.24
TiO_2	1.84	Ce	358.7	Tm	0.3	Pb	37.44
Al_2O_3	13.91	Pr	36.2	Yb	1.7	Rb	163.7
FeO*	6.13	Nd	127.7	Lu	0.2	Cs	5.58
MnO	0.1	Sm	19.8	Ba	1658	Sr	1215
MgO	2.57	Eu	3.9	Th	32.4	Sc	9.7
CaO	6.26	Gd	11.6	Nb	51.6	Zr	584
Na_2O	3.09	Tb	1.4	Y	28.6		
K_2O	3.99	Dy	6.8	Ni	19		
P_2O_5	0.98	Ho	1.1	Cr	28		

A.

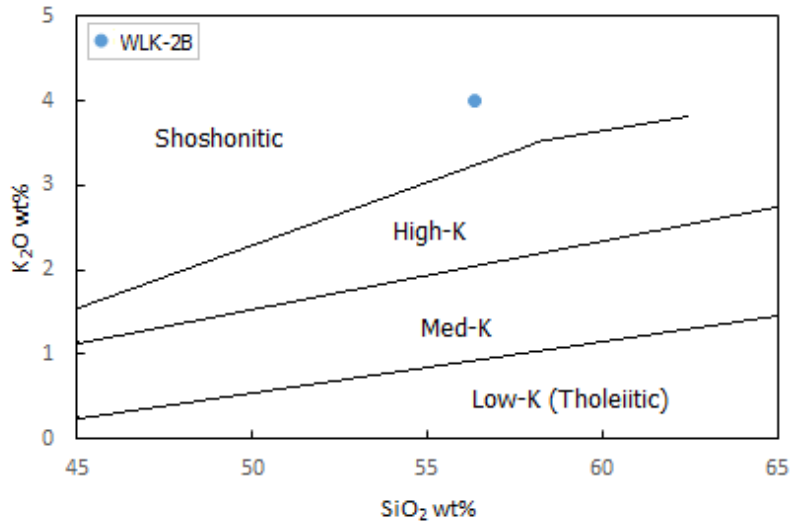

B.

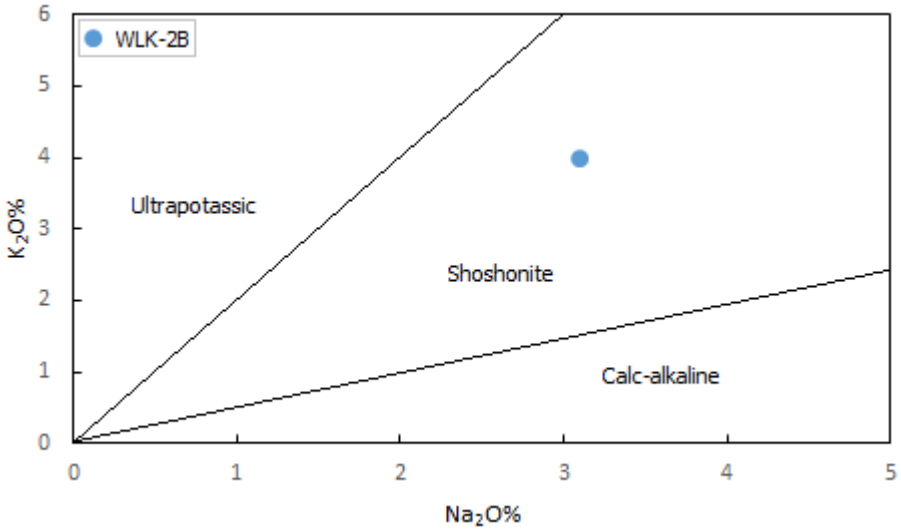

Fig. 17. (A) K_2O versus SiO_2 plot with WLK-2B whole rock sample plotting in Shoshonite field. (B) K_2O versus Na_2O plot with WLK-2B whole rock sample plotting in Shoshonite field (Modified from Best, 2003).

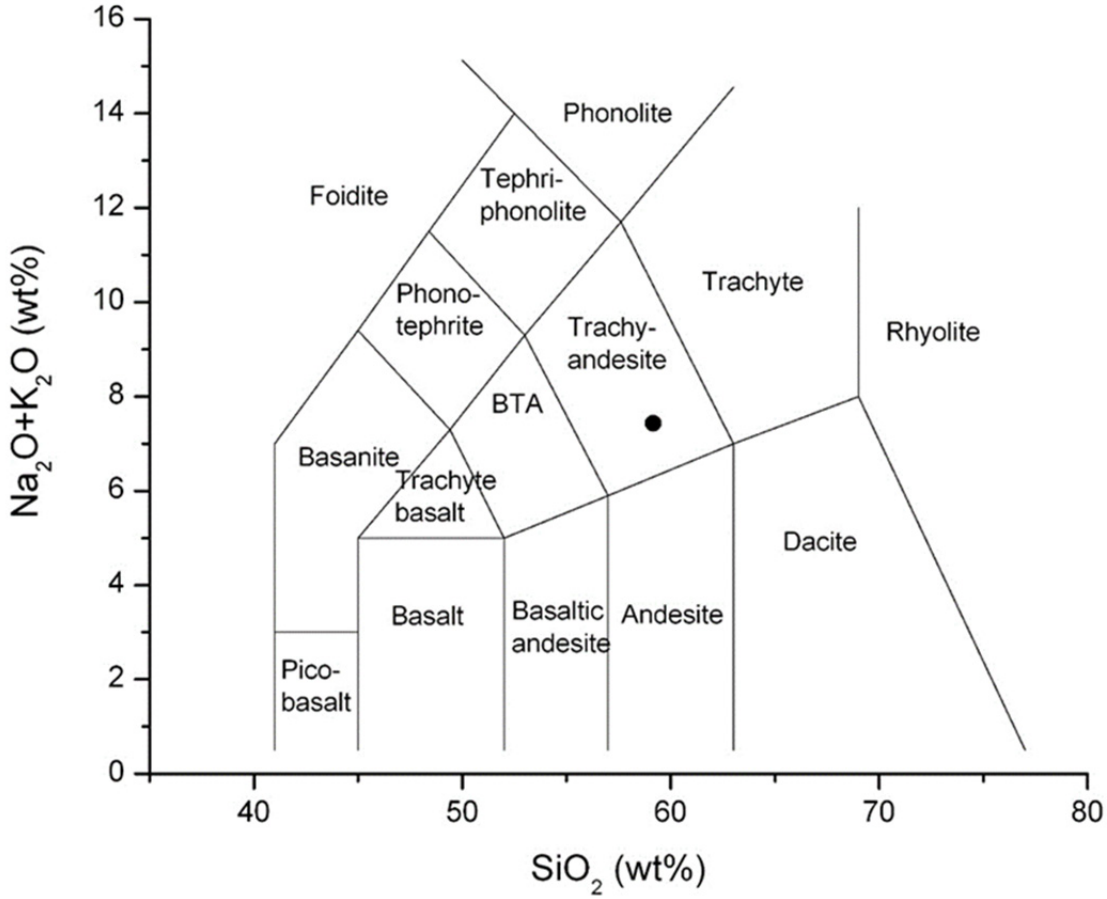

Fig. 18. Total alkali-silica plot indicating a trachyandesite composition of the WLK-2B whole rock sample (From Le Bas et al., 1986).

Spider and REE diagrams (Figs. 19 and 20) must be normalized because the concentrations of individual elements are too variable to display and because of the odd-even effects. Normalization will also make changes in concentrations easier to interpret than absolute concentrations. The REE plot is normalized using element concentrations in carbonaceous chondrites (CI), while the spider diagram is normalized using average primitive mantle (McDonough and Sun, 1995).

Whole rock analysis of WLK-2B shows high LREE enrichment and a negative slope on the REE plot. The REE pattern displays a slight negative Eu anomaly. Negative Eu anomalies are likely a result of plagioclase separating from the magma during fractional crystallization. This anomaly is consistent with petrographical observation of abundant plagioclase phenocrysts.

Plotted trace element patterns show enrichment in most incompatible elements and depletions in Nb and Ta. The spider diagram shows a strong negative Nb and Ta anomaly. The the negative Sr anomaly in the spider diagram also is consistent with the fractional crystallization of plagioclase. This sample has low Nb/U and Ce/Pb ratios and plots below the ocean island basalt (OIB) field as shown in figure 21.

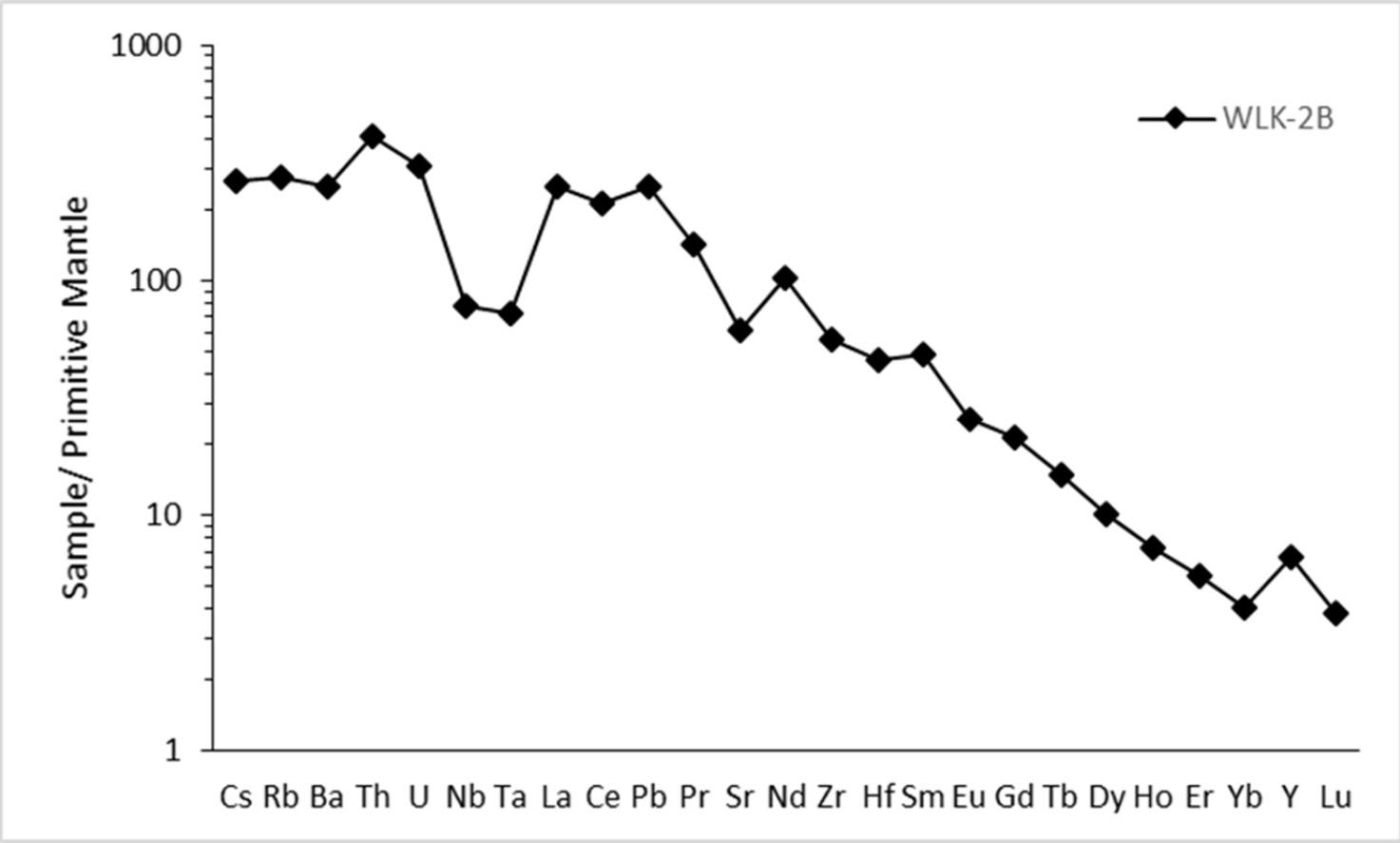

Fig. 19. Spider diagram of trace elements from WLK-2B whole rock sample. The vertical axis is normalized using estimated primitive mantle (From McDonough and Sun, 1995).

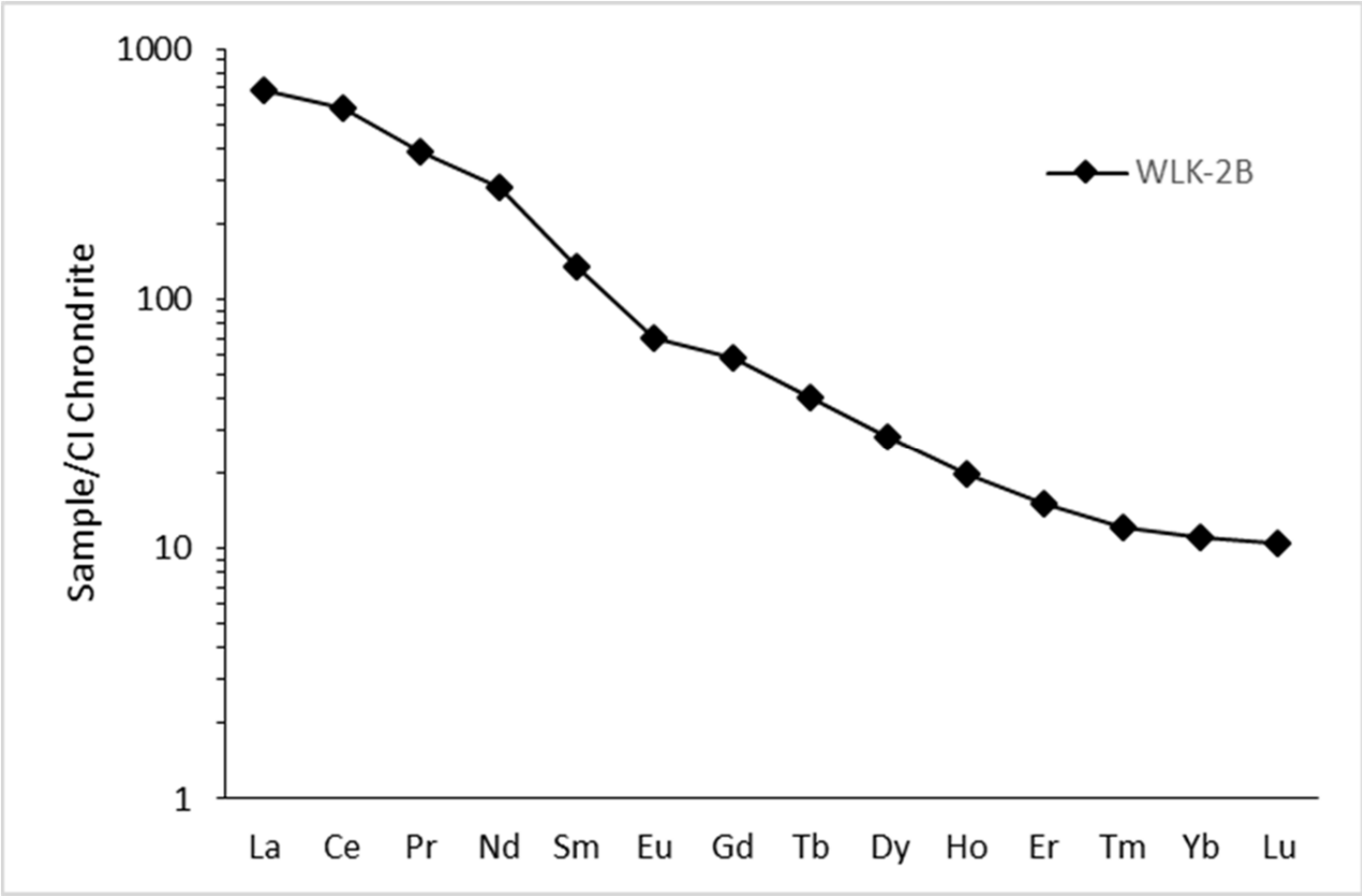

Fig. 20. REE plot of WLK-2B whole rock sample. The vertical axis is normalized using carbonaceous chondrite (From McDonough and Sun, 1995). The negative slope indicates enrichment in LREEs.

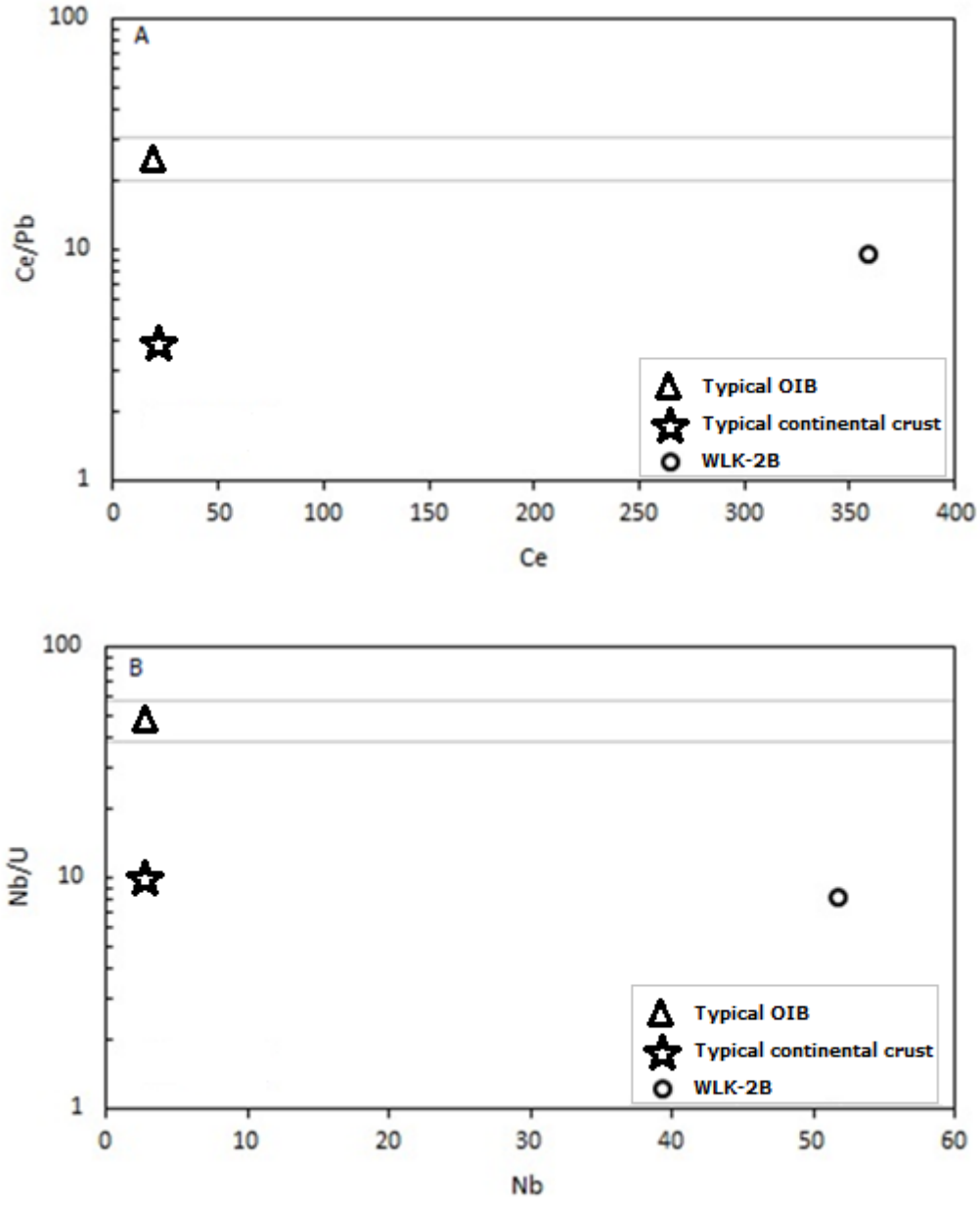

Fig 21. (A) Ce/Pb ratios versus Ce concentrations. (B) Nb/U ratios versus Nb concentrations of WLK-2B whole rock (Modified from Zou et al., 2000).

Electron Microprobe Analysis

Data collected from the electron microprobe are shown in Tables 3, 4 and 5. The WLK-2B sample consists primarily of OPX and plagioclase feldspar phenocrysts with accessory minerals of zircon, ilmenite and apatite. The matrix consists of glass and microscopic feldspar. The data collected from the feldspar phenocrysts were plotted on an An-Ab-Or diagram (Fig. 22A). The diagram shows that all measured feldspar phenocrysts are andesines. The An value of the plagioclase phenocrysts is 30-40 which is acidic and in equilibrium with the melt. (Yu et al., 2014). The data collected from the OPX phenocrysts were plotted on an En-Fe-Wo diagram (Fig. 22B). The diagram indicates that the OPX phenocrysts range from bronzite to hypersthene but hypersthene is predominant. The OPX phenocrysts are Mg rich with En values of 59-69. These analytical results from the OPX and feldspar phenocrysts are consistent with those represented for the Ashi volcano (Yu et al., 2014).

Due to the lack of co-existing 2-pyroxenes, 2-feldspars, or Fe-Ti oxides in the trachyandesite prevents the use of conventional geothermometers to determine the magma temperature prior to eruption (Zou et al., 2010b). Additionally, the lack of co-existing Fe-Ti oxides prevents the calculation of oxygen fugacity**.** As a consequence, recently developed orthopyroxene-liquid geothermometry and plagioclase-liquid geothermometry (Putirka, 2008) were used to estimate magma temperature. Temperatures from four different OPX-glass pairs were calculated and then averaged producing an average magma temperature of about 1000 ºC. Temperatures from four different plagioclase-glass pairs were also calculated and then averaged producing an average magma temperature of about 1040 ºC. Typical uncertainties for these

geothermometers are about 30 ºC. Temperatures estimated from the plagioclase-glass geothermometer appear to be slightly higher than those from the orthopyroxene-liquid geothermometry, but both temperature estimates are still within the 30 ºC uncertainties. These high similar temperatures suggest that the OPX and plagioclase crystals are early-formed phenocrysts.

Table 3.
Electron microprobe analysis of pyroxene phenocrysts in Wuluke volcano rock (in wt%).

Thin section	Pyroxene number	Mineral	SiO_2	TiO_2	Al_2O_3	Cr_2O_3	MgO	CaO	MnO	FeO	Na_2O	K_2O	Total	Wo	En	Fs
WLK-2B-2	Pyroxene1	OPX	49.24	0.57	3.34	0	21	1.92	0.36	21.67	0.08	0	98.2	3.97	60.8	35.24
	Pyroxene2	OPX	49.51	0.71	2.95	0	21	2.43	0.47	20.37	0.1	0.01	97.6	5.08	61.6	33.35
	Pyroxene3 rim	OPX rim	49.38	0.53	3.05	0.03	20.1	2.16	0.43	22.43	0.05	0.01	98.2	4.51	58.7	36.77
	Pyroxene3 core	OPX core	49.69	0.76	3.25	0.03	22.9	1.95	0.42	18.08	0.21	0	97.3	4.06	66.5	29.46
	Circle2 Pyroxene 1	OPX	46.68	0.38	7.01	0.03	19.8	0.17	0.09	22.69	0.03	0	96.9	0.37	60.7	38.92
	Circle3 Pyroxene 1	OPX	51.15	0.59	2.06	0.1	24.7	2.43	0.47	16.79	0.1	0	98.3	4.82	68.9	26.26
WLK-2B-1	Pyroxene1	OPX	49.75	0.62	2.32	0	21.4	3.31	0.41	20.24	0.09	0.02	98.2	6.73	61	32.3

Table 4.
Electron microprobe analyses of feldspar phenocrysts in WLK-2B (in wt%).

Thin Section	Feldspar Number	Mineral	SiO_2	TiO_2	$Al2O_3$	MgO	CaO	MnO	FeO	Na_2O	K_2O	Total	Ab (Na)	Or (K)	An (Ca)
WLK-2B-2	Feldspar1a	Pl	57.81	0.03	25.28	0.04	7.46	0.09	0	6.78	0.59	98.11	60.36	3.36	36.27
	Feldspar2a	Pl	59.04	0.05	24.69	0	7.06	0.05	0.12	6.87	0.74	98.66	61.05	4.21	34.74
	Plagioclase2 rim	Pl rim	58.19	0.05	24.97	0	7.29	-0.09	0.05	6.26	1.44	98.19	55.76	8.37	35.86
	Plagioclase2 core	Pl core	57.82	0	25	-0.01	6.86	-0.05	0.1	6.37	1.66	97.74	56.64	9.63	33.72
	Circle2 feldspar3a	Pl	58.43	0.03	25.8	0	7.44	0	0	6.11	1.32	99.17	55.09	7.77	37.13
	Circle2 feldspar3b	Pl	56.2	0.1	25.6	0	8.08	-0.09	0.04	6.23	1.26	97.45	54.11	7.2	38.69
	Circle2 feldspar4	Pl	56.83	0.07	24.92	0.02	7.94	-0.07	0.45	5.78	1.26	97.24	52.64	7.52	39.84
	Circle3 feldspar1	Pl	59.12	0.02	24.19	0.04	5.78	-0.06	0.1	7.85	0.99	98.06	67.17	5.55	27.27
WLK-2B-1	Feldspar1	Pl	58.19	0.02	25.35	0	7.08	0.03	0.16	7.05	0.7	98.61	61.79	4.01	34.2
	Feldspar2	Pl	58.49	0	24.05	0	5.82	0.03	0.12	7.55	0.85	96.92	66.71	4.9	28.39

Table 5.
Electron microprobe analyses of ilmenite and glass in WLK-2B (in wt%).

Thin Section	Number	Mineral	SiO_2	TiO_2	Al_2O_3	MgO	CaO	MnO	FeO	K_2O	Na_2O	Total
WLK-2B-2	ilmenite1	ilmenite	0	47.96	0.14	3.74	0.12	0.31	42.29	0	0	94.56
WLK-2B-1	ilmenite2	ilmenite	0.15	47.46	0.043	3.22	0.16	0.81	42.27	0	0	94.113
WLK-2B-2	glass1	glass	63.32	1.73	15.19	0.65	2.91	0.07	3.24	4.88	2.78	94.77
WLK-2B-2	glass2	glass	63.79	1.31	17.83	0.05	3.13	0.06	1.72	4.93	3.59	96.41
WLK-2B-2	glass3	glass	63.57	1.49	16.68	0.99	3.23	0	3.69	4.17	3.15	96.97
WLK-2B-2	glass4	glass	64.06	1.44	16.08	0.41	3.03	0	3.12	3.78	3.25	95.17
WLK-2B-1	glass1	glass	65.92	2.08	15.54	0.2	2.54	0	2.58	4.56	2.74	96.16
WLK-2B-1	glass2	glass	65.12	1.43	17.17	0.21	2.87	0.03	1.98	4.41	3.14	96.36

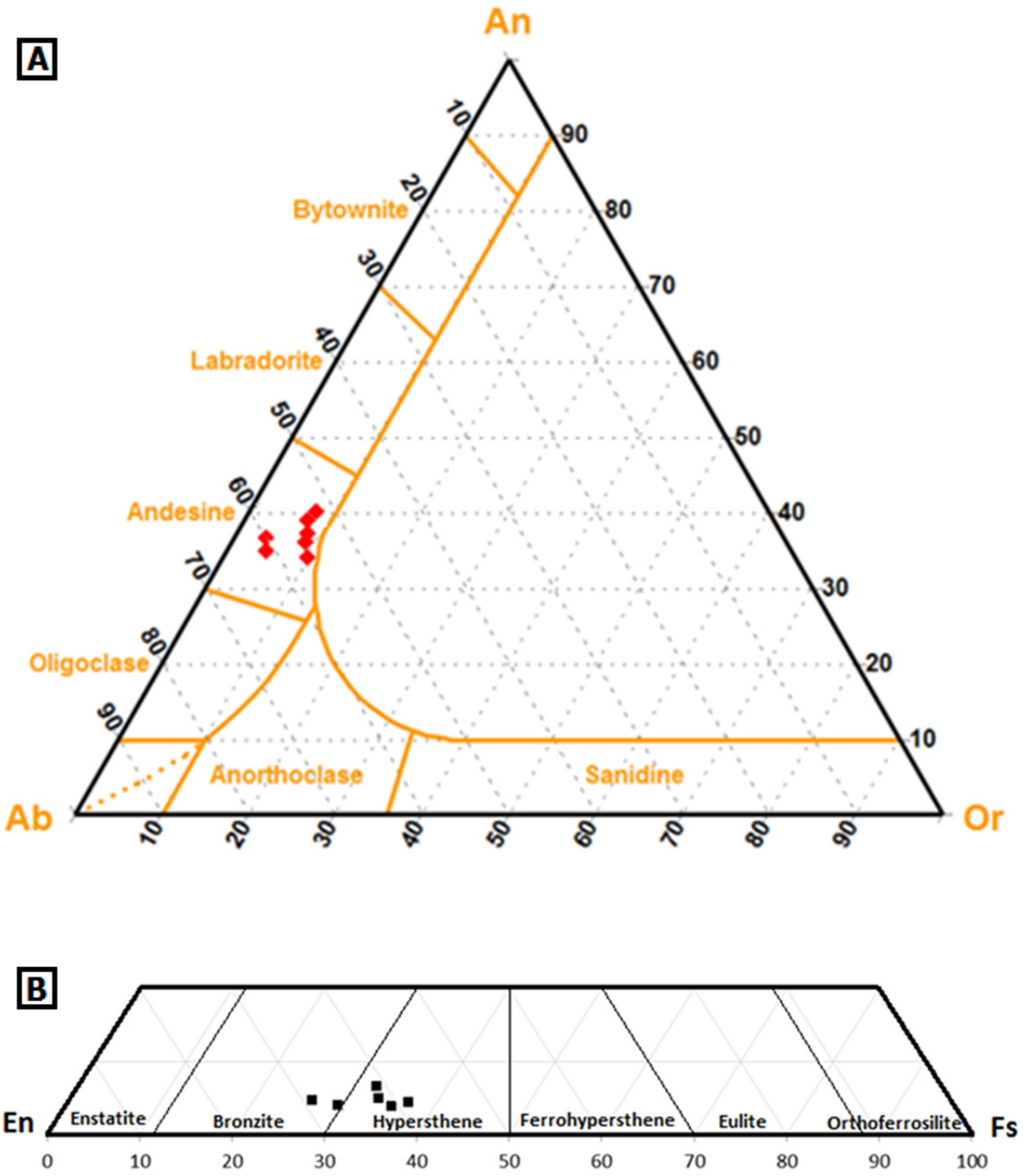

Fig. 22. (A) Classification of feldspar using tertiary Ab-An-Or plot of O'Connor (1965). (B) Classification of orthopyroxene of Yu et al. (2014).

SIMS Data

Sixty-eight polished zircons were measured by SIMS to obtain ^{238}U-^{206}Pb ages (Table 6). The ages were then plotted in a histogram (Fig. 23) showing counts versus age. Figure 23 shows that the Wuluke zircons do not represent a single age population and instead there are many separate age populations. The ages were also plotted on a concordia plot shown in Figure 24. Although Paleoproterozoic zircons are discordant, the younger zircons are concordant. The age populations range from the most recent eruption (~.2 ka) to the Paleoproterozoic (~2600 Ma). The youngest age population (~.2 Ma) shows the largest number of counts. This age population correlates well with previously K-Ar dated samples from the Wuluke volcano used to identify the Wuluke episode of volcanism associated with the AVC (Liu and Maimaiti, 1989). These .2 Ma zircons are phenocrysts that crystallized from the host magmas. Zircons significantly older than .2 Ma are interpreted as assimilated xenocrysts from the basement and country rock.

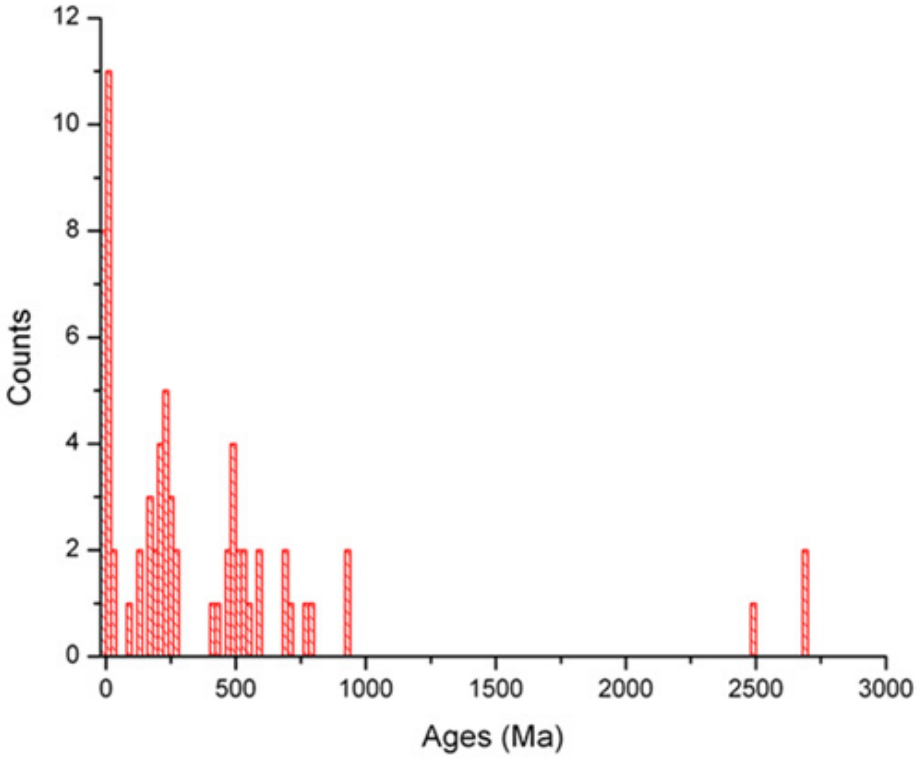

Fig. 23. Counts versus zircon U-Pb ages obtained from 68 zircons measured using SIMS.

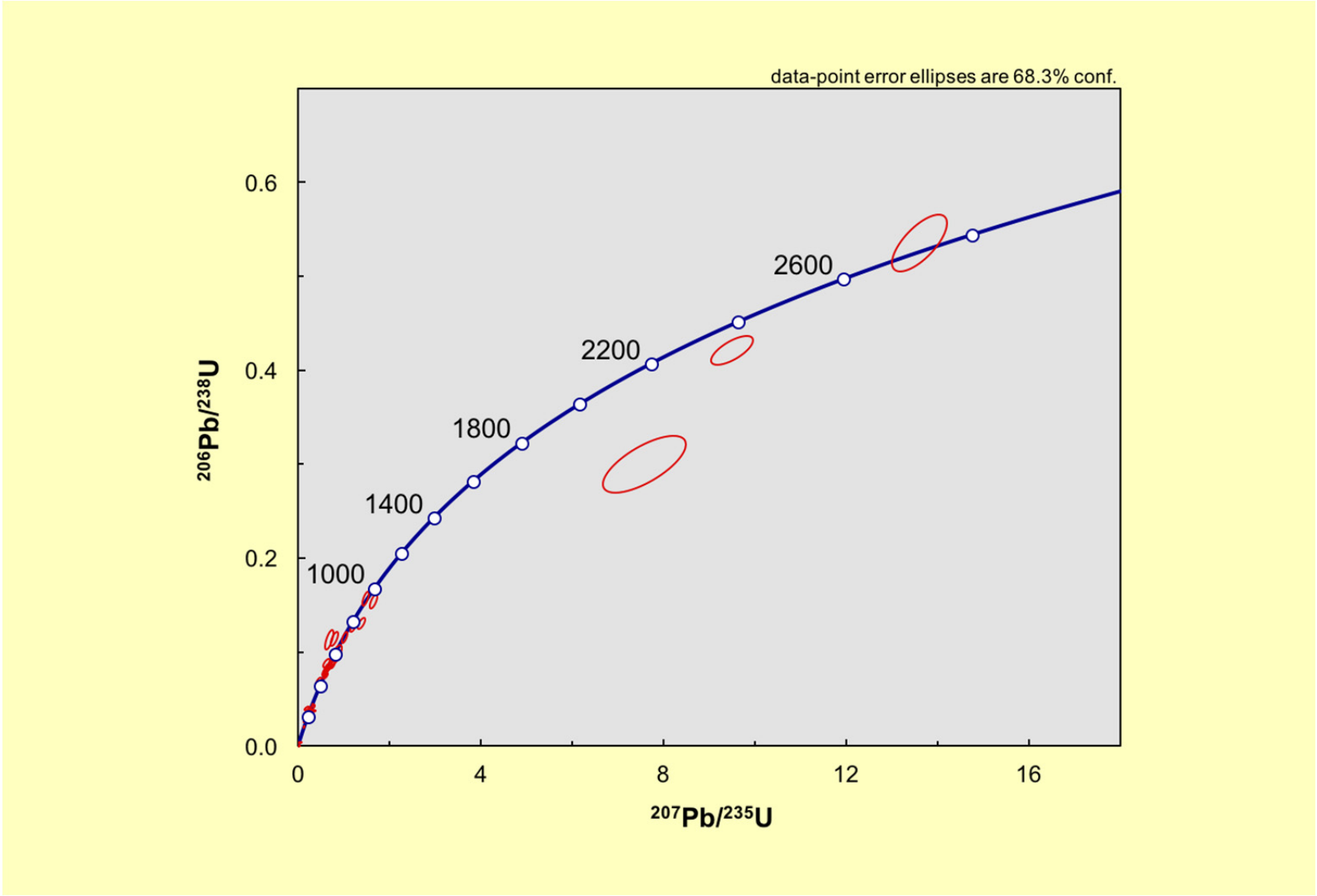

Fig. 24. U-Pb concordia plot of zircon ages obtained from 68 zircons measured using SIMS.

Table 6.
U/Pb isotope data and ages for Wuluke zircons measured by SIMS.

Sample	Age (Ma)	Age (Ma)	Age (Ma)	Age (Ma)	Age (Ma)	Age (Ma)	U O/U	Common	Common	Common
	$^{206}Pb/^{238}U$	$^{206}Pb/^{238}U$	$^{207}Pb/^{235}U$	$^{207}Pb/^{235}U$	$^{207}Pb/^{206}Pb$	$^{207}Pb/^{206}Pb$		$^{206}Pb/^{204}Pb$	$^{207}Pb/^{204}Pb$	$^{208}Pb/^{204}Pb$
		1 s.e.		1 s.e.		1 s.e.				
WLK_B@4.ais	132	3.76	123.2	9.28	-1	0.00327	6.56	18.86	15.62	38.34
WLK_B@5.ais	210.9	6.83	202.6	7.15	106.7	47.4	6.27	18.86	15.62	38.34
WLK_B@6.ais	597.1	39.8	618.9	45.1	699.3	78.7	6.12	18.86	15.62	38.34
WLK_B@7.ais	792.1	22.4	881.8	21	1114	24.9	6.63	18.86	15.62	38.34
WLK_B@8.ais	2266	61.6	2388	29.2	2493	7.43	6.31	18.86	15.62	38.34
WLK_B@9.ais	493	15.4	465.9	15.5	334.6	63.4	6.35	18.86	15.62	38.34
WLK_B@10.ais	204	6.48	189.9	11.2	17.72	136	6.24	18.86	15.62	38.34
WLK_B@11.ais	199.1	7.24	201.2	29.5	226	353	6.1	18.86	15.62	38.34
WLK_B@14.ais	539.4	15.8	576.4	17.1	725.2	51.5	6.57	18.86	15.62	38.34
WLK_B@15.ais	922.8	26.6	989	22.2	1139	21.2	6.56	18.86	15.62	38.34
WLK_B@16.ais	132.9	3.91	121.9	11.1	-1	0.00387	6.54	18.86	15.62	38.34
WLK_B@17.ais	764.3	18.1	802	17.4	908.4	32	6.72	18.86	15.62	38.34
WLK_B@19.ais	689.5	41.1	526.9	35.8	-1	0.00253	5.68	18.86	15.62	38.34
WLK_B@20.ais	487.2	15.2	477.9	12.8	433.7	39.1	6.38	18.86	15.62	38.34
WLK_B@21.ais	525.1	13.9	541.8	17.1	612.6	52.9	6.58	18.86	15.62	38.34
WLK_B@22.ais	519.2	15.3	512.3	15.7	481.8	47.9	6.32	18.86	15.62	38.34
WLK_B@23.ais	474.2	12.8	472.4	12.7	464.1	44.6	6.46	18.86	15.62	38.34
WLK_B@24.ais	582.4	17.4	598.9	18	661.9	50.2	6.27	18.86	15.62	38.34
WLK_B@25.ais	0.569	0.976	2.659	17.9	2947	8.31E+03	6.17	18.86	15.62	38.34
WLK_B@27.ais	236	8.33	227.8	9.89	144	73.1	6.05	18.86	15.62	38.34
WLK_B@28.ais	175.6	6.69	144.4	22.3	-1	0.00632	6.26	18.86	15.62	38.34
WLK_B@29.ais	508.6	16.2	493.7	14.1	425.4	38.7	6.29	18.86	15.62	38.34
WLK_B@30.ais	413.8	13.4	418.9	15.5	447	62.8	6.44	18.86	15.62	38.34
WLK_B@32.ais	1690	112	2184	72	2687	18	6.08	18.86	15.62	38.34
WLK_B@33.ais	708	22.9	712.8	18.3	728.2	24	6.14	18.86	15.62	38.34
WLK_B@35.ais	697.9	30.7	592.6	27	207.6	80.8	5.69	18.86	15.62	38.34
WLK_A@1.ais	0.3257	0.322	0.6007	6.11	1314	1.79E+04	6.22	18.86	15.62	38.34

Table 6 continued.
U/Pb isotope data and ages for Wuluke zircons measured by SIMS.

Sample	Age (Ma)	Age (Ma)	Age (Ma)	Age (Ma)	Age (Ma)	Age (Ma)	U O/U	Common	Common	Common
	$^{206}Pb/^{238}U$	$^{206}Pb/^{238}U$	$^{207}Pb/^{235}U$	$^{207}Pb/^{235}U$	$^{207}Pb/^{206}Pb$	$^{207}Pb/^{206}Pb$		$^{206}Pb/^{204}Pb$	$^{207}Pb/^{204}Pb$	$^{208}Pb/^{204}Pb$
		1 s.e.		1 s.e.		1 s.e.				
WLK_A@4.ais	0.3738	0.325	0.2406	6.06	-1	0.722	6.31	18.86	15.62	38.34
WLK_A@5.ais	229.1	6.98	213.2	7.42	40.65	53.5	6.24	18.86	15.62	38.34
WLK_A@7.ais	229.7	8.93	254.3	59.2	487	549	6.21	18.86	15.62	38.34
WLK_A@9.ais	545.5	20	485.4	29	210.7	152	6.23	18.86	15.62	38.34
WLK_A@10.ais	937.3	26.3	919.1	20	875.7	24.8	6.29	18.86	15.62	38.34
WLK_A@11.ais	245.4	7.29	239	6.84	176.6	26	6.25	18.86	15.62	38.34
WLK_A@12.ais	188.8	7.37	180.1	17.5	67.32	235	6.22	18.86	15.62	38.34
WLK_A@13.ais	23	0.825	21.79	2.11	-1	0.00388	6.11	18.86	15.62	38.34
WLK_A@17.ais	259.8	12.7	277.7	20	431	128	5.69	18.86	15.62	38.34
WLK_A@19.ais	208.9	6.61	241	26	567.1	241	6.52	18.86	15.62	38.34
WLK_A@20.ais	223.8	6.31	220	10.7	180.4	93.3	6.51	18.86	15.62	38.34
WLK_A@21.ais	0.4038	0.048	0.6128	0.815	925.5	2.51E+03	6.54	18.86	15.62	38.34
WLK_A@22.ais	483.1	14.4	445.3	15.7	254.7	63.7	6.42	18.86	15.62	38.34
WLK_A@23.ais	273.6	8.02	277.5	9.54	310.7	58.8	6.44	18.86	15.62	38.34
WLK_A@24.ais	2764	67.7	2724	29.6	2695	9.65	6.42	18.86	15.62	38.34
WLK_BGM@1.ais	1.239	0.807	13.99	14.5	4309	661	7.05	18.86	15.62	38.34
WLK_BGM@3.ais	229.1	5.8	230.1	15.9	240	159	6.74	18.86	15.62	38.34
WLK_BGM@5.ais	467.4	10.2	476.9	17.3	522.8	83.2	7.15	18.86	15.62	38.34
WLK_BGM@6.ais	171.4	5.79	199.6	52.8	548.1	599	6.59	18.86	15.62	38.34
WLK_BGM@7.ais	22.59	4.79	18.08	39.2	-1	0.0774	6.98	18.86	15.62	38.34
WLK_BGM@9.ais	491.6	10.7	472.7	11.5	382.1	38.8	6.97	18.86	15.62	38.34
WLK_BGM@10.ais	205.8	5.15	181.8	9.48	-1	0.00208	6.88	18.86	15.62	38.34
WLK_BGM@11.ais	254	7.23	178.9	27	-1	0.00542	6.71	18.86	15.62	38.34
WLK_BGM@12.ais	429.8	20.1	379.7	24.7	84.65	170	7.42	18.86	15.62	38.34

DISCUSSION

Zircon Age Populations

U-Pb isotope dating of 68 zircons from sample WLK-2B measured multiple age populations ranging from the most recent eruption (~.2 Ma) to the Paleoproterozoic (~2600 Ma). As shown in Figure 23 and 24, the cluster of younger ages (~.2 Ma) suggest that these zircons are phenocrysts that crystallized from the host magmas. Additionally, these measured ages correspond well with previously K-Ar dated samples (.2-.12 Ma) from the Wuluke volcano (Liu and Maimati, 1989).

In addition to the host magma zircon phenocrysts, U-Pb isotope dating detected many Proterozoic age zircons in WLK-2B. Several of the zircon age populations are as old as the surrounding country rock. Many of the WLK-2B age peaks correlate well with that of the Tarim craton. The basement and country rocks underlying the Tarim crust consist of Late Archean and Paleoproterozoic rocks which were emplaced in multiple phases including 500-800 Ma and 2.5-2.8 Ga (Zhang et al., 2013). Since the zircons from WLK-2B correlate well with rocks of these ages, it is likely that these zircons were captured from the basement and country rock. Other old zircons whose ages do not correlate with known basement ages were likely entrained from local wall rocks from the Kunlun mountains during magma ascent. Most of the zircons are concordant. However, some xenocryst zircons in the 2.5-2.8 Ga age population are discordant and plot below the concordia curve. This discordant array is a result of Pb-loss which is likely indicative of the xenocryst zircons' metamorphic origins.

Zircon Saturation

Determining whether the magma was saturated with respect to zircon is important when trying to interpret possible zircon inheritance from country rock. However, due to the abundance of phenocrysts and old zircons in WLK-2B, it is safe to assume that the melt was saturated in Zr and inherited zircons were stable in the melt after being entrained from the country rock. This study will use zircon saturation temperature to determine where along the temperature evolution of the magma that inherited zircons become stable within the melt. Due to the low Zr solubility in peraluminous melts, zircon saturation levels are significantly lower than in non-peraluminous melts. Zircon saturation is a function of both temperature and magma composition and is defined by the following relationship (Watson and Harrison, 1983):

$$lnD_{Zr}^{Zircon/melt} = \{-3.80 - [0.85(M-1)]\} + \frac{12900}{T}$$

Where $D_{Zr}^{Zircon/melt}$ is the concentration ratio of Zr in zircon to that in the melt. T is the absolute temperature in Kelvins, and M represents melt composition of (Na+K+2Ca)/(Al*Si). Rearranging the equation to T_{Zr} yields the zircon saturation temperature for the melt:

$$T_{Zr} = 12900/[2.95 + .85M + \ln\left(\frac{496{,}000}{Zr_{melt}}\right)]$$

According to the WLK-2B major element compositions, M= 2.68. The calculated zircon saturation temperature is 804 ºC. So once the melt reached the zircon saturation

temperature of 804 ºC, the inherited zircons, as a result of crustal contamination, would remain stable and not re-dissolve into the melt.

Crustal Contamination

Zircons entrained in mantle-derived magmas offer a unique opportunity to assess mantle and crustal evolution (Liu et al., 2013). Determining if the Wuluke volcanic rocks contain xenocrystic zircons is important for several reasons. Zircon xenocrysts from mantle-derived rock can be used as potential probes of crustal evolution. Additionally, determining if the zircons have a xenocrystic origin can also contribute information regarding the extent and nature of crustal contamination.

The abundance of old zircons provides compelling evidence that WLK-2B contains xencrystic zircons from assimilated country rock from the crust. The assimilated country rock provided an abundance of xenocrystic zircons and possibly some SiO_2, but it is unlikely to have significantly contributed to the chemical composition of the magma. The enriched mantle source of the magma is responsible for the enriched characteristics of the whole rock, and is not a result of crustal contamination. Additionally, the similar estimated temperatures and lack of zoning along the rims of the early formed OPX and plagioclase phenocrysts indicate that the phenocrysts remained in equilibrium with the melt which was not significantly affected by crustal contamination. Earlier contamination, or recycling of material within the lithospheric mantle, is potentially responsible for some of the enriched characteristics. However, because xenocrystic zircons would likely of been re-dissolved at these temperatures, further whole rock Sr,

Nd, and Pb isotopic data is required to place better constraints on contamination processes within lithospheric mantle.

Magma Origin and Evolution

Based on whole rock concentrations, the Wuluke rock has been identified as a trachyandesite. Trace and major element data indicate enriched mantle characteristics. This is supported by the negative Nb and Ta anomalies. Mid-ocean ridge basalts (MORB) and ocean island basalts (OIB) typically have positive Nb and Ta anomalies, so a MORB mantle source can be ruled out as a magma source. Since Nb and Ta are also typically low in subduction-related melts, the negative Nb and Ta anomaly may also be indicative of partial melting of a mantle source metasomatized by hydrous fluids. LREE enrichment further indicates an enriched mantle source. Additionally, rocks with high K_2O are unlikely to have been derived from the asthenosphere and instead are characteristic of an enriched mantle source. Lavas from the volcanoes within the Ashikule basin likely share a common source. Based on Nd isotopic ratios from Cooper et al., (2002), rock samples from the Ashikule basin have negative ε_{Nd} values ranging from -6.66 to -7.32. These negative values suggest that the enrichment in incompatible elements is a characteristic of an enriched mantle source (Cooper et al., 2002). It is likely that the lavas from the Wuluke volcano were formed by partial melting of an enriched sub-continental lithospheric mantle (SCLM).

Magma temperatures of 1000 ºC and 1040 C have been estimated for the Wuluke sample (WLK-2B) based on orthopyroxene-liquid geothermometry and plagioclase-liquid geothermometry (Purtika, 2008). These high temperatures indicate that the OPX

and plagioclase phenocrysts are early formed crystals. Due to the lower zircon saturation temperature, it is likely that OPX and plagioclase phenocrysts crystallized first while zircon crystallized at a lower temperature. The negative Sr and Eu anomalies may relate to the fractional crystallization of plagioclase. The negative Eu anomaly is subtle, which may suggest that the fractional crystallization of plagioclase played a minor role in the evolution of the magma. During the magma's ascent, the melt experienced crustal contamination by the assimilation of zircon bearing country rock. This is supported by the abundance of zircon xenocrysts in the country rock. At the zircon saturation temperature of 804 ºC, the entrained zircons would have remained stable within the peraluminous Zr-saturated melt.

CONCLUSIONS

(1) U-Pb isotope dating of zircons with SIMS documents that the WLK-2B sample has multiple zircon age populations. The ages range from the most recent eruption to the Proterozoic. The Proterozoic ages correlate well with known basement and country rock ages indicating that the WLK-2B sample contains both phenocryst and xenocryst zircons.

(2) Interpretation of major and trace element whole rock data suggests that the trachyandesite lavas from the Wuluke volcano were formed by partial melting of an enriched mantle source.

(3) Results from this study provide strong evidence that the lavas from the Wuluke volcano have experienced crustal contamination through the assimilation of zircon-bearing country rocks. Crustal contamination may not significantly affect the chemical equilibrium between major minerals and the melt.

REFERENCS

Armstrong, J.T., 1988, *Quantitative analysis of silicate and oxide minerals: Comparison of Monte Carlo, ZAF, and Phi-Rho-Z procedures, in Microbeam Analysis*: D.E. Newbury, ed., San Francisco, California, San-Francisco Press, 239-246.

Best, M.G., 2003. *Igneous and Metamorphic Petrology*, 2nd ed.: Blackwell Publishing, Massachusetts, 729 pp.

Bi, H., Wang, Z., Wang, Y., Zhu X., 1999. History of tectono-magmatic evolution in the western Kunlun orogen. Science in China (Series D) 42.6, 604-619.

Chatterjee, S., Goswami, A., Scotese, C., 2013. The longest voyage: Tectonic, magmatic, and paleoclimate evolution of the Indian plate during its northward flight from Gondwana to Asia. Gondwana Research 23.1, 238-267.

Compston, W., Williams, I.S., C. Meyer., 1984. U-Pb Geochronology of zircons from lunar breccia 73217 using a sensitive high mass-resolution ion microprobe. Journal of Geophysical Research: Solid Earth 89, 525-534.

Cooper, K. M., Reid, M. R., Dunbar, N. W., Mcintosh, W. C., 2002. Origin of mafic magmas beneath northwestern Tibet: Constraints from ^{230}Th- ^{238}U Disequilibria. Geochemistry, Geophysics, Geosystems 3.11, 1-23.

Dewey, J., Shackleton, R., Chengfa, C., Yiyin, S.,1988. The tectonic evolution of the Tibetan plateau. The Royal Society. http://dx.doi.org/10.1098/rsta.1988.0135

Finch, R.J., Hanchar, J.M., 2003. Structure and chemistry of zircon and zircon-group minerals. *In* Zircon, Reviews in Mineralogy & Geochemistry 53 (J.M. Hanchar, and P.W.O. Hoskin, eds.). The Mineralogical Society of America, Washington, 1-25.

Harrison, T. Mark, Watson, E. Bruce., Aikman, B. Aikman., 2007. Temperature spectra of zircon crystallization in plutonic rocks. The Geological Society of America 35.7, 635-638.

Hoskin, P.W.O., Schaltegger, U., 2003. The composition of zircon and igneous and metamorphic petrogenesis. *In* Zircon, Reviews in Mineralogy & Geochemistry 53 (J.M. Hanchar, and P.W.O. Hoskin, eds.). The Mineralogical Society of America, Washington, 27-62.

Ireland, T. R., Williams, I.S., 2003. Considerations in zircon geochronology by SIMS. Reviews in Mineralogy and Geochemistry 53.1, 215-241.

Košler, J., Sylvester, P.J., 2003. Present trends and the future of zircon in geochronology: Laser Ablation ICPMS, *In* Zircon, Reviews in Mineralogy & Geochemistry 53 (J.M. Hanchar, and P.W.O. Hoskin, eds.). The Mineralogical Society of America, Washington, 243-275.

Le Bas, M.J., Le Maitre, R.W., Streckeisen, A., Zanettin, B., 1986. A chemical classification of volcanic rocks based on the total alkali-silica diagram. Journal of Petrology 27, 745-750.

Liu, D., Zhao, Z., Zhu, D., Niu, Y., Harrison, T., 2013. Zircon xenocrysts in Tibetan ultrapotassic magmas: imaging the deep crust through Time." Geology 42.1, 43-46.

Liu, J., Maimaiti, Y., 1989. Distribution and ages of Ashikule volcanoes on the west Kunlun Mountains, west China. Bulletin of Glacier Research 7, 187-90.

McDonough, W. F., Sun, S.S., 1995. The composition of the Earth. Chemical Geology 120, 223-253.

O'Connor, J. T., 1965. A classification for quartz-rich igneous rocks based on feldspar ratios. US Geological Survey Professional Paper B525. USGS, 79–84.

Putirka, K. D., 2008. Thermometers and barometers for volcanic systems. Reviews in Mineralogy and Geochemistry 69.1, 61-120.

Scherer, E. E., Whitehouse, M.J., Munker, C., 2007. Zircon as a monitor of crustal growth. Elements 3, 19-24.

Stern, R.A., 2009, Chapter 1: An introduction to secondary ion mass spectrometry (SIMS) in geology. Mineralogical Association of Canada Short Course 41, Toronto, 1-18.

Tapponnier, P., Lacassin, R., Leloup, P.H., Scharer, U., Zhong, D.L., Wu, H.W., Liu, X.H., Ji, S.C., Zhang, L.S., Zhong, J.Y.,1990. The Ailao Shan/Red River metamorphic belt: tertiary left-lateral shear between Indochina and South China. Nature, 343, 431–437.

Tapponnier, P., Zhigin, X., Roger, F., Meyer, B., Arnaud, N., Wittlinger, G., Jinqsui, Y., 2001. Oblique stepwise rise and growth of the Tibet plateau. Science 294(5547), 1671-1677.

Tucker, R. T., 2011. U-Th Dating of zircons from a Holocene volcanic eruption (Dayingshan Volcano, Tengchong Volcanic Field): Insights into magma chamber storage. MS Thesis. Auburn University, Alabama.

Tucker, R. T., Zou, H. B., Fan, Q. C., Schmitt, A. K., 2013. Ion microprobe dating of zircons from active Dayingshan volcano, Tengchong, SE Tibetan Plateau: time scales and nature of magma chamber storage. Lithos 172-173, 214-221.

"UGA Microprobe Lab Home Page." http://www.gly.uga.edu/railsback/SpeleoLabProbe1.html. Accessed August 10, 2015.

"UCLA SIMS Home Page." http://sims.ess.ucla.edu/index.php. Accessed August 10, 2015.

Wang, E., Wan, J., Liu, J., 2003. Late Cenozoic geological evolution of the foreland basin bordering the West Kunlun range in Pulu area: Constraints on timing of uplift of northern margin of the Tibetan Plateau. Journal of Geophysical Research. http://dx.doi.org/10.1029/2002JB001877.

Watson, E.B., Harrison, T.M., 1983. Zircon saturation revisited: temperature and composition effects in a variety of crustal magma types. Earth and Planetary Science Letters 64, 295-304.

Xia, L.Q., Li, X.M., Ma, Z.P., Zu, X.Y., Zia, Z.C., 2011. Cenozoic volcanism and tectonic evolution of the Tibetan plateau. Gondwana Research, 19, 850–866.

Xu, J., Zhao, B., Zhang, L., Chen, Z., 2012. Field geological exploration of the Ashikule Volcano group in western Kunlun Mountains. Earthquake Research in China 26, 152-159.

Yu, H., Xu, J., Zhao, B., Shen, H., Lin, C., 2014. Magmatic processes of Ashi Volcano, western Kunlun Mountains, China. Acta Geologica Sinica, English Edition 88.2, 530-43.

Zhang, C.L., Zou, H.B., Li, H.K., Wang, H.Y., 2013. Tectonic framework and Evolution of the Tarim block in NW China. Gondwana Research 23.4, 1306-1315.

Zhao, M., 1976. Introduction on Ashikule active volcanoes and the Quaternary volcano groups in Kunlun Mountains of Xinjang. Xinjang Geology 1-2, 27-36.

Zou, H.B., Zindler, A., Xu, X., Qi, Q., 2000. Major, trace element, and Nd, Sr and Pb isotope studies of Cenozoic basalts in SE China: mantle sources, regional variations, and tectonic significance. Chemical Geology 171(1-2), 33-47.

Zou, H.B., 2007. *Quantitative Geochemistry*: Imperial College Press, London, 291 p.

Zou, H.B., and Fan, Q.C., 2010. U-Th isotopes in Hainan basalts: Implications for sub-asthenospheric origin of EM2 mantle endmember and the dynamics of melting beneath Hainan Island. Lithos 116, 145-152.

Zou, H.B, Fan, Q., Zhang, H., 2010a. Rapid development of the great Millennium eruption of Changbaishan (Tianchi) Volcano, China/North Korea: Evidence from U–Th zircon dating. Lithos 119, 289-96.

Zou, H.B., Fan, Q.C., Schmitt, A.K., Sui, J.L., 2010b. U-Th dating of zircons from Holocene potassic andesites (Manshan volcano, Tengchong, SE Tibetan Plateau) by depth profiling: Time scales and nature of magma storage. Lithos 118, 202-210.